FINITE ELEMENT MODELING TO PREDICT BULK MECHANICAL PROPERTIES OF 3D PRINTED METAL FOAMS

Report Master Thesis

M.S. Borleffs, student

Supervisors: Dr. A.A. Zadpoor and G. Campoli

Supervising professor: Prof.dr.ir. H.H. Weinans

Department of Biomechanical Engineering,

Faculty of Mechanical, Maritime and Materials Engineering,

Delft University of Technology (TU Delft),

Mekelweg 2, Delft 2628 CD, The Netherlands

Correspondence, email:

m.s.borleffs@student.tudelft.nl,

tel: +31 6 19742649

Keywords: Metal foam; Bulk mechanical properties; Finite element method; Additive manufacturing

Word count: 6723

Submission date 25.10.2012

ABSTRACT

Worldwide yearly 800.000-1.000.000 people receive a total artificial hip. 8-9% Of all patients requires a second surgery to correct the primary arthroplasty. In more than 70% of cases, aseptic loosening is the cause for implant failure. Possible pathways leading to aseptic loosening are stress shielding and micro-motions. Stress shielding can be reduced by less stiff implant material in the susceptible areas and micro-motions can be minimized by a stable fixation in the bone, e.g. due to bone ingrowth into the implant. Three dimensional (3D) printing techniques provide the possibility to combine solid metal with metal foam in one implant. The apparent density (AD) of the foam is in direct relation with the Young's modulus, so the stiffness of the foam can be tailored with the AD. The printing does entail imperfections in the foam, such as irregular cross-sections of the struts and porosity within the struts. Analytical models are based on the perfectly regular situation and therefore do not satisfy in the prediction of the foam stiffness. A custom-made finite element (FE) modeling tool was developed to generate models of metal foams that do include these irregularities. The struts were all composed of several beam elements to which different cross-section sizes were assigned based on a Gaussian distribution. In addition, porosity within the struts was modelled by assigning a void percentage to the matrix material, which was also Gaussian distributed. In this study, the predicted bulk mechanical properties of models generated with the modeling tool were compared to analytical models and to experimental results in order to validate the FE results. It was shown that FE modeling is a promising method to predict the stiffness of 3D printed metal foams. Especially the stiffness of foams with a low AD was properly predicted by the FE model. Further development is required to optimize the accuracy of the outcome. It is recommended to include non axial alignment of the beam elements. In the future, FE modeling can be used to optimize the geometrical and mechanical properties of patient specific implants.

LIST OF ABBIRVATIONS

THA	-	total hip arthroplasty
AM	-	additive manufacturing
3D	-	three dimensional
SEBM	-	selective electron beam melting
SLM	-	selective laser melting
CAD	-	computer aided design
FE	-	finite element
GUI	-	graphical user interface
FEM	-	finite element method
AD	-	apparent density
CB	-	cube
DM	-	diamond
TO	-	truncated octahedron
RD	-	rhombic dodecahedron
SD	-	standard deviation
SEM	-	scanning electron microscope
CS	-	cross-section

TABLE OF CONTENT

1. INTRODUCTION

1.1. BACKGROUND

Total hip arthroplasty (THA) is a widely used surgical procedure. In patients suffering from osteoarthritis, traumatic fracture, or other problems with their hip joint, it is one of the most developed and successful surgical interventions, resulting in immediate pain relief and reinstatement of the patient's mobility [1, 2]. In general, the acetabular part consists of a shell and liner and the femoral part is formed by a stem and head.

Since 1979, Sweden has a national total hip arthroplasty register, recording all primary THA, THA revisions and the corresponding surgical techniques and environmental aspects [3, 4]. Register data show that annually 13.000 total hip arthroplasties are performed in Sweden [5]. Worldwide this number is estimated at 800.000-1.000.000 [1, 6, 7], with a predicted growth of 200% in the next 20 years, due to increasing age and lifestyle changes of the population [1, 8]. According to the Swedish Hip Register during 1995-2000, in 8-9% of cases second surgery to correct the primary THA was needed [5, 9]. These include all revisions, regardless of the time after initial implantation. Worldwide this results in an estimated 64.000-72.000 revision surgeries annually. These numbers stress the importance to improve THA.

In more than 70% of cases, aseptic loosening is the cause for implant failure, often occurring relatively late after implantation [5, 10]. Important causes of aseptic loosening are micro-motions and stress shielding. Micro-motions occur when the implant is free to slide in the modullary canal. It can be a result of too little bone ingrowth or malpositioning of the implant [11]. In general, instability of the implant often causes early revision [10]. Stress shielding occurs when the implant is too stiff compared to the original bone. The implant carries part of the loading that is no longer experienced by the surrounding bone. This changes and reduces the stress sustained by the bone and results in remodeling of the surrounding bone. According to Wolff's law, which explains the adaptation of bone to the loads it experiences, bone resorption occurs as a result of stress shielding. Resorption leads to a lower bone density and eventually loosening of the implant [12].

Titanium and its alloys are the most commonly used metals for the femoral stem [13]. The advantages of metals are their overall good mechanical properties, leading to a relatively low wear rate [14]. Besides solid titanium, porous titanium/titanium foam is used in biomedical applications. The porosity of the titanium is related to the Young's modulus of the structure [15]. A higher porosity results in a lower Young's modulus, so less stiff material.

With the current possibilities of additive manufacturing (AM), a titanium implant can be printed three dimensional (3D) with a previously prescribed geometry, microstructure and consequently, mechanical properties. In some areas titanium foam can be applied, and in others solid titanium. It is even possible to print foam with a negative Poisson's ratio, causing compressive stress to be experienced by the surrounding bone, even when tensile loading occurs [16]. The foam variables (e.g. type of unit cell, strut length and radius of the strut cross-section) and resulting apparent density can vary throughout the implant. A custom-made implant can be created based on the specific requirements of the patient. An implant with optimal mechanical and geometrical properties in each location will reduce stress shielding and micro-motions.

1.2. PRINTING PROCESS OF TITANIUM FOAM

Open-cell titanium structures can be produced by AM techniques, the two most common ones being selective electron beam melting (SEBM) and selective laser melting (SLM). As stated by Van Bael *et al.* [17], additive manufacturing techniques provide, due to the layer-wise building method and their direct link with a computer aided design (CAD) model, the ability to produce porous structures with controlled pore and strut dimensions. The procedure of the product generation by SEBM is described in Figure 1. SEBM is a technique, using an electron beam to selectively melt metal powder layer by layer. Each layer is formed by a powder bed, in which selective areas are solidified due to the melting and create a cross-section of the eventual product. After a layer is melted, the process platform moves vertically downwards, a new layer of powder is applied, and a new layer can be melted. When the generation of the product is completed, all unmelted powder is recycled. The resolution in the first two directions is determined by the size of the powder particles. For titanium alloy (Ti-6Al-4V) powder, the particles are spherical and have sizes between 25 and 80 µm [17-19]. In SEBM the resolution of the table is reported to be 70 µm [19] or 100 µm [18]. The main difference between SLM and SEBM is the energy source. In SLM, a laser beam is guided through an optical fibre and is focussed on selective areas in the powder bed to solidify these by melting.

Currently, analytical models are used to predict the stiffness of 3D printed metal foams. These models are based on the flawless situation and do not include irregularities, such as varying radius of the cross-section of the struts. However, regularity cannot be guaranteed in AM techniques.

1.3. THE AIM OF THE STUDY

The purpose of the current study is to use finite element modeling for prediction of bulk mechanical properties of metal foams based on the geometrical properties of the foam. The models were generated with a special

developed tool for Abaqus (SIMULIA, Providence, RI), in which effects of manufacturing imperfections can be included that are not included in the stiffness prediction by analytical models.

2. MATERIALS AND METHODS

In order to fulfill the objective of the study, convergence, parametric and comparative studies were performed on finite element models of titanium foam. The current chapter describes the used materials and methods.

2.1. FE MODEL

All finite element (FE) models were generated using a custom-made graphical user interface (GUI), which is depicted in Figure 2. The models represented titanium foam microstructures, composed of regularly stacked unit cells. The struts of the foam were modelled as beams. The number of elements per strut could be defined through *number of edge divisions*. All elements were 2-node linear beam elements (B31). This element is the standard Timoshenko beam element and allows for transverse shear deformation [20]. Displacement boundary conditions in three orthogonal planes were applied to model uniaxial compression tests and stabilize the structures. In all models, the strain was applied in direction [1,0,0]. An input- and par-file were automatically generated; those served as the input for the post-processing script. The par-file contains the dimensions and deformation of the model, while the input-file contains all other finite element method (FEM) data such as boundary conditions and loading.

After the post-processing script had run, a text file was created with the resulting bulk mechanical properties Young's modulus (E) and Poisson's ratio (ν), and the apparent density (AD) of the foam. The Young's modulus and Poisson's ratio indicate the stiffness of a structure. The Young's modulus is the initial slope of the linear part of the stress-strain curve. The Poisson's ratio is defined by the negative ratio of transverse contraction strain to axial extension strain. A material with a Poisson's ratio of 0.5 is considered incompressible. The Young's modulus and Poisson's ratio of the matrix material were based on the material properties of Ti-6Al-4V and were standard set at 110 GPa and 0.3, respectively. The shear modulus (G) and bulk modulus (K) of an isotropic material can be derived when the Young's modulus and Poisson's ratio are known [21]. Together these four properties define the mechanical behaviour of an isotropic material.

$$E = \frac{\sigma}{\varepsilon}, \qquad \nu = -\frac{\varepsilon_{trans}}{\varepsilon_{axial}}, \qquad G = \frac{E}{2(1+\nu)}, \qquad K = \frac{E}{3(1-2\nu)}$$

The Young's modulus and Poisson's ratio of the foam were obtained by compressing the foam with 0.2% strain. The post-processing script computed the effective Young's modulus and Poisson's ratio as proposed by Li *et al.*

(2006) [22]. In the presented formulas the stain is applied in direction [1,0,0] and X,Y,Z are the dimensions of the foam model. F_1 is the total reaction force along direction [1,0,0] and u^i_j is the lateral displacement in the x_j direction perpendicular to the loading direction x_i. The apparent density is calculated by dividing the volume of all beams over the volume of the total structure.

$$E_1 = \frac{-F_1}{\varepsilon_1 YZ}, \qquad v_{12} = -\frac{u_2^1}{\varepsilon_1 Y}, \qquad v_{13} = -\frac{u_3^1}{\varepsilon_1 Z}, \qquad AD = \frac{\sum V_{beam}}{V_{total}}$$

In the GUI, several foam parameters can be defined. The main parameters are the unit cell geometry (cube (CB), diamond (DM), truncated octahedron (TO) or rhombic dodecahedron (RD), represented in Figure 3), beam length, radius/edge length of the beam cross-section (depends if the cross-section is a circle or square), void percentage within the beams and dimensions of the complete foam. Models that are composed of diamond, truncated octahedron or rhombic dodecahedron unit cells all contain beams with a circular cross-section, so cylindrical beams. Only for models composed of cube unit cells, prismatic beams are an option as well, so with a square cross-section.

The truncated octahedron, diamond and clearly the cube have cubic symmetries. As a result the mechanical properties of these models are equal in three principal directions [23]. The rhombic dodecahedron has three orthogonal planes of symmetry [20]. Therefore, the mechanical properties in [0,1,0] and [0,0,1] direction are the same, but differ from the mechanical properties in [1,0,0] direction. Since the strain was standard in [1,0,0] direction, the Young's modulus is also computed for this direction. Unless explicitly mentioned otherwise, the values in Table 1 were the standard input.

In analytical models of foams, the cross-section of the struts of the unit cells is considered equal throughout the structure. In the GUI, this corresponds to a fixed radius/edge length of the beams. However, these models with fixed strut radius appear to be too stiff compared to experimental results of foam samples [18]. As observed by Parthasarthy *et al.*, increased structural variations in small strut sizes might result in thin structures that result in failure at lesser loads [18]. As a consequence of the manufacturing process, the diameter of the beams varies throughout the foam. Figure 5 shows several images of the microstructure of titanium foam where the irregularity of the beam cross-section can be seen. In order to model the varying cross-sections of the struts, the GUI includes an option for a Gaussian distribution of the radius or edge length of the cross-section. Figure 6 visualizes the meaning of a Gaussian or normal distribution of the cross-section size. A cross-section size is assigned to each different element and is picked from a limited range that is defined

by the mean section size, standard deviation (SD) of the size and a Gaussian filter. The filter guarantees that the section size stays within a sensible, printable range. Due to the Gaussian distribution, sizes close to the mean occur more frequent than away from the mean. A total number of variations can be set by the user, called *number of sections*. The SD defines the width of the variations. When the threshold is reached, the radius is recalculated.

Another effect of the manufacturing technique that may occur is porosity within the struts. This was observed in foam samples with cube unitcells with prismatic struts [18]. Figure 5a shows an image of such a sample where the dark spots represent void. Porosity within the struts can be modelled by assigning a void percentage with SD to the matrix material, leading to a lower Young's modulus.

2.1.1. Fixed radius/edge length

First, FE models with fixed radius were studied on the structural level. These models indicated the relation between the variables of the microstructure and its mechanical properties Young's modulus and Poisson's ratio. The apparent density according to the FEM data was first validated in this section. Formulas were derived to calculate the AD of the cube (1) and truncated octahedron (2) models. The variables that defined the AD were the length (L), beam radius (r) and number of unit cells (n).

$$\rho = \frac{v_f}{v_t}, \qquad f = foam, \qquad t = total$$

$$\rho_{CB} = \frac{3\pi r^2 L n^3 + 9\pi r^2 L n + (n-1)6\pi r^2 n L}{(nL)^3} \qquad (1)$$

$$\rho_{TO} = \frac{36\pi r^2 L n^3 - 12\pi r^2 L n^2 (n-1)}{\left\{\left(\sqrt{2} + 2\sqrt{\frac{1}{2}}\right) L n\right\}^3} \qquad (2)$$

The validation of the AD was followed by a convergence study on the size of the model, to obtain the number of unit cells required for a predictable, stable stiffness of the foam. A parametric study was performed by analyzing the influence of the parameters size and radius on the mechanical properties. Models of each type of unit cell were created with an increasing number of unit cells in each dimension. The beam length and radius were fixed, length at 1.2 mm and radius once at 0.01 mm to generate slender models, and once at 0.25 mm to generate models with a standard beam radius. For the rest of the report, when a model contained 10 unit cells, it means the models contained 10 unit cells *in each dimension.* To study the parameter radius, models with varying beam radius were generated with the other parameters fixed according to the standard input (Table 1)

and the size fixed at 10 unit cells. In case of the cube models with a square cross-section of the beams, the edge length had the same value as the radius of the beam in the other geometries.

The outcome of the FE models with a fixed cross-section size was compared to analytical models in order to validate the predicted stiffness.

2.1.2. Gaussian distribution of the radius

Second, FE models with a Gaussian distribution of the cross-section radius were analyzed. The influence of the number of unit cells and SD of the mean radius on the predicted stiffness was evaluated. FE models were created with an increasing number of unit cells (2, 5 and 10). The other parameters were fixed. Each model was regenerated ten times. Similar to the models with fixed radius, the standard input parameters were used (Table 1). Furthermore, the beam radius was defined as follows:

$$Beam\ mean\ section\ size = 0.25\ mm, \qquad SD = 0.02\ mm, \qquad filter = 2$$

The influence of the SD of the mean radius was analyzed by generating models with an increasing SD and keeping the other variables fixed. The maximum SD in the parametric study was based on the assumption that 0.1 mm was the minimal printable radius. Since the mean radius was set at 0.25 mm and the filter on 2, this minimum led to a maximum SD of 0.75 mm. The smallest SD was chosen 0.05 mm and the SD increased with 0.1 mm per model. Each model was regenerated ten times.

$$Threshold = filter \cdot SD$$

$$Mean\ beam\ radius = 0.25\ mm, \qquad min.radius = 0.10\ mm \rightarrow\ max.radius = 0.40\ mm$$

$$With\ filter = 2, maximum\ SD = 0.075\ mm$$

Models with a Gaussian distributed strut radius were expected to represent experimental samples, because these include irregularities which occur in reality. In order to analyze the accuracy of the stiffness prediction with FE modeling, experimental results of Ti-6Al-4V foam samples were compared to results of corresponding FE models with a Gaussian distribution of the radius and a possible porosity within the struts. Throughout the study, the GUI was optimized and the steps were iterated. The method that was used in this study is visualized in Figure 4.

2.2. ANALYTICAL MODELS

Now the generation method of the FE models is explained, the data that was used from literature to validate the FEM data shall be discussed. The stiffness predication of FE models with a fixed strut radius was validated with the aid of analytical models. No analytical model could be found for diamond as a unit cell. Analytical

models are generally developed for infinitely large structures, so the analytical solutions were not influenced by the number of unit cells. The following analytical models were used. More information about them can be found in Appendix 8.1.

Cube (cylindrical beams): Gent and Thomas (1963) [24]

Young's modulus: $E_f = \frac{E_s \beta^2}{1+\beta}$

Apparent density: $\rho = \frac{3\beta^2 + \beta^3}{(1+\beta)^3}$

Poisson's ratio: $\nu = 0$

Cube (prismatic beams): Gent and Thomas (1963) [24]

Young's modulus: $E_f = \frac{E_s \beta^2}{1+\beta}, \quad \beta = \frac{a}{L}, \quad a = edge\ length\ CS, \quad L = beamlength$

Poisson's ratio: $\nu = 0$

Truncated Octahedron: Roberts and Garboczi (2002) [25]

Young's modulus: $E_\mathrm{f} = \frac{2}{3} E_s C_z \rho^2 (1 + C_z \rho)^{-1}$

Poisson's ratio: $v_{12} = \frac{1}{2}\left(\frac{1 - C_z\rho}{1 + C_z\rho}\right)$

$C_z = 0.900\ for\ struts\ with\ circular\ cross-section$

Rhombic Dodecahedron: Babaee et al. (2012) [20]

Young's modulus: $E_{f,1} = \frac{E_s \frac{27 \sin\theta}{\sin 2\theta}}{\frac{3L^4}{\pi r^4} + \frac{18L^2}{\pi r^2}}, \quad \theta = 54.73°$

$E_{f,3} = E_s \frac{9\pi r^4 \cos\theta}{2L^4 \sin^2\theta}$

Poisson's ratio: $\nu_{13} = 0, \nu_{12} = 1$

$\nu_{31} = \nu_{32} = 0.5$

2.3. EXPERIMENTAL DATA FROM THE LITERATURE

In order to evaluate the outcome of FE models with a Gaussian distribution of the radius, their outcomes were compared to experimental data from literature on Ti-6Al-4V foam samples. No experimental data could be

found for truncated octahedron as a unit cell. The relation between the Young's modulus and AD was evaluated for the experimental data and for the FEM data. In order to simulate the experimental samples with the FE models, the input parameters for the FE models were the same as the parameters of the experimental samples (Table 2). According to the supplier of the matrix material, the Young's modulus of Ti-6Al-4V was 120 GPa [26]. The displacement boundary conditions in XY-plane and XZ-plane were removed, so only the plane opposite to the applied strain was constrained and the real geometry of the samples was used in the FE models. The samples with diamond and rhombic dodecahedron unit cells had cylindrical struts and a printing layer thickness of 70 µm. The samples with cube unit cells had prismatic struts and a printing layer thickness of 100 µm. The minimum and maximum radius of the cross-section of the strut was measured in a sample with rhombic dodecahedron unit cells produced by SLM. The measurements were done by Saber Amin Yavari with the scanning electron microscope (SEM) at the TU Delft. From these measurements, a ratio of the SD over the mean radius of 1:6 could be determined. This ratio was used to determine the SD of the radius in the FE models with diamond and rhombic dodecahedron unit cells. The chosen SD of the edge length in the models with cube unit cells was based on the best fit. Porosity within the struts was only observed in the struts of the samples with cube unit cells (Figure 5). In the FE models, the total material volume is determined by summing the volume of each beam. However, in reality beams are overlapping at the intersections. This double-counted volume becomes more significant as the AD increases. FE models of the intersecting beams with corresponding radii were created to determine the double-counted volume and recalculate the correct AD. The correction of the AD can be found in Appendix 8.2. The stiffness of the different FE models was compared to the corresponding experimental results to analyze the accuracy of the prediction and whether the FE prediction is an improvement compared to the analytical prediction.

Cube: Parthasarathy et al. (2010) [18]

Parthasarathy *et al.* produced four different samples sets by SEBM, with seven cubic samples each (15x15x15 mm^3) which were all composed of cube unit cells with a square cross-section of the struts [18]. All FE models had mean edge lengths corresponding to the experimental data and 10-20% (SD 0.025) porosity within the beams. Models with a maximum SD of the edge length were generated, and with an SD as reported by Parthasarathy *et al.* [18]. The maximum SD was based on a minimal printable edge length of 0.1 mm. This SD was 20 times larger than the reported SD.

Diamond: Heinl et al. (2008) [19]

Heinl *et al.* investigated cellular titanium that was manufactured by SEBM as developed by Arcam AB and was built from diamond unit cells [26]. An important difference between Heinl's experimental data and our FEM data is the fact that Heinl has determined the *dynamic* elastic modulus and in the FE models the *static* elastic modulus is computed. Both moduli are determined by the slope of the linear part of the stress-strain curve, but the dynamic elastic modulus is the slope from data obtained under vibratory conditions, while the static elastic modulus is obtained under static conditions. Heinl had determined the dynamic elastic modulus by the impulse excitation technique, wherefore rectangular bars were used (62.5x11.0x14.5 mm^3). The numerical difference between the *dynamic* and *static* moduli of Ti-6Al-4V has been studied by Lee *et al.* (1991) [27]. They investigated the influence of the process temperature on both moduli. The specimens in Heinl's study were manufactured at 970°C [26]. At this temperature, the *static* elastic modulus was found to be 2% lower than the *dynamic* elastic modulus.

Rhombic Dodecahedron: LayerWise (tests performed August 2012)

The company LayerWise produced cylindrical titanium foam samples by SLM with rhombic dodecahedron unit cells. LayerWise performed compression tests and shared their data with us. Four different sample sets were produced and tested, with five cylindrical samples each. They all had the same dimensions (height 15 µm and diameter 10 µm), but varied in beam length and beam radius, and consequently in AD. The reported Young's modulus was assumed to be the modulus in the first direction, so determined by compression in [1,0,0].

3. RESULTS

In this chapter the results of the study will be presented. First, the results are reported of the convergence study and parametric studies on the FE models with a fixed strut radius and with a Gaussian distribution of the strut radius. Second, the comparisons between FEM data and analytical data, and FEM data and experimental data are reported.

3.1. CONVERGENCE STUDY AND PARAMETRIC STUDY

3.1.1. Fixed radius

The hand calculations of the AD and the output of the FE models led to the exact same numbers (Table 3). This comparison provided a validation of the AD as given in the FE results.

Figure 7a and b show plots with the Young's modulus as a function of the number of unit cells for each type of unit cell and with beam radius 0.25 mm. The influence of the size on the Young's modulus in slender models

(radius 0.01 mm) can be found in the Appendix 8.3 (Figure 13). Figure 14 in Appendix 8.3 illustrates the Poisson's ratio as a function of the number of unit cells for each geometry and a strut radius of 0.25 mm. As expected from the hand calculations, an increasing number of unit cells resulted in a decreasing AD. For each geometry, the Young's modulus converged to the modulus that the foam had if it was infinitely large. However, the truncated octahedron was stiffer with fewer cells and the diamond and rhombic dodecahedron were stiffer with more cells. This is caused by the structural instability of the diamond and rhombic dodecahedron unit cells. For example, the single diamond unit cell has loose ends, which require connection to another unit cell to attain stability. The Young's modulus of the rhombic dodecahedron jumped up and down as a result of the shape of the unit cell and how the unit cells are stacked. If a line would connect the centres of the rhombic dodecahedron unit cells in a two dimensional plane, it resulted in a zigzag pattern instead of a straight line. The number of unit cells did not influence the stiffness of the models with cube unit cells. On this scale, the deformation purely led to compression of the perfectly aligned struts and no detectable cell edge bending. In the other three types of unit cells, bending of the cell edges dominated the mechanical properties.

For the diamond and the rhombic dodecahedron (v_{13}), the influence of the number of unit cells on Poisson's ratios is comparable to its influence on the Young's modulus: the ratios converge to a certain number. However, the Poisson's ratios of the truncated octahedron and rhombic dodecahedron (v_{12}) are quite messy. No transverse strain could be detected in the cube models due to the perfectly aligned struts; this resulted in Poisson's ratios of zero.

Concluding, the number of unit cells that is required for a predictable and stable stiffness is displayed in Table 4. The displayed quantities are based on the fact that an extra unit cell changes the predicted property by less than 1, 5 or 10%. Assuming less than 1% change defines a stable Young's modulus, the cube requires at least 2 unit cells, diamond 10, truncated octahedron 6 and rhombic dodecahedron 18. For a stable Poisson's ratio, 2 cube unit cells are required and 20 diamond unit cells. It should be taken into account that these numbers are for structures with strut length 1.2 mm and strut radius 0.25 mm.

Figure 7e depicts the Young's modulus as a function of the radius for each geometry and Figure 7c and d the Poisson's ratio as a function of the radius. An increasing radius resulted in an increasing Young's modulus for each type of unit cell. This was a predictable result, since a higher radius (when keeping strut length constant), means stronger material and thus, higher stiffness. When the structure gets bulkier, there is more resistant to deformation and the connections between the unit cells are more solid.

The Poisson's ratios actually decreased with an increasing radius. This corresponds to the increasing Young's modulus. A stiffer structure can deform less, leading to smaller transverse strains in relation to the axial strain, resulting in a lower Poisson's ratio. As mentioned before, a material with a Poisson's ratio of 0.5 is considered incompressible. When the ratio is less than 0.5 (e.g. in models with truncated octahedron unit cells and a high AD), it means the transverse strain is smaller than half the axial strain, so less transverse deformation is allowed.

3.1.2. Gaussian distribution of the radius

In the next paragraph, the parametric study is reported that evaluated the influence of the number of unit cells and SD of the mean radius on the predicted stiffness of models with a Gaussian distributed strut radius. The influence of the number of unit cells on the Young's modulus in models with a Gaussian distribution of the cross-section radius was similar to models with a fixed radius. The plots for the different geometries increased or decreased initially to converge to a certain modulus. Due to the irregularities in the microstructure, the models with a Gaussian distribution of the cross-section radius were less stiff than the models with a fixed radius and as a consequence all data slightly shifted downwards in the plots. When the number of unit cells increases, more displacement modes are possible; this leads to a higher SD of the Young's modulus. In contrast, the structures become more stable as the size increases, resulting in a lower SD of the mechanical property. These effects seem to compensate each other, because no trend in the SD of the property could be observed.

The Poisson's ratios of the models with a Gaussian distribution of the cross-section radius varied negligible with the ratios of the models with fixed radius. The SD of the Poisson's ratio was very small and no trend could be observed as an effect of the increment of the number of unit cells. Plots of the mechanical properties against the size can be found in the Appendix 8.3.1 (Figure 15 and Figure 16), the corresponding data in Appendix 8.3.2 (Table 6).

Increasing the SD of the beam radius resulted in a lower Young's modulus. When the SD is large, very small and large radii can occur in the model. The small radii dominated the Young's modulus and were not cancelled out by the large radii. The increasing SD of the Young's modulus is due to the rising possibilities of radius combinations. When different radii are randomly distributed over the cross-sections of the struts, weaker spots with thin struts and stiffer struts with thick struts will be created. At the weaker spots, failure will occur at lesser loads, resulting in reduced bulk mechanical properties. The rising possible combinations of the strut thicknesses lead to a higher variety of moduli.

For each type of unit cell, the Poisson's ratio slowly increased when increasing the SD of the beam radius. More deformation is allowed when the structures are less stiff, leading to higher Poisson's ratios. Also the SD of the Poisson's ratio increased, caused by the rising possible displacement modes. Plots of the relation between the SD and the mechanical properties are shown in Figure 8, the corresponding data can be found in Appendix 8.3 (Table 7). The error bars indicate the SD of the property on the Y-axis.

3.2. COMPARISON WITH ANALYTICAL SOLUTIONS

All analytical models were based on an infinitely large structure, so the analytical solutions were not influenced by the number of unit cells and were therefore represented by a line. The comparison is depicted in Figure 7. Tables of the datasets can be found in the Appendix 8.3 (Table 6, Table 7, Table 8, Table 9, Table 10, Table 11 and Table 12). All compared analytical models especially fitted the slender FE models, so models with low apparent densities. This can be explained by the fact that the analytical models are based on the most simplified situation. When the beams are slender, shear stress and torsion can be ignored and Timoshenko's theory can be applied. The variation between the analytical solution and the FE solution indeed increased as the strut radius of the beams increased, while the strut length was kept constant.

Since the analytical solution for the stiffness of models with cube unit cells was not influenced by the size of the model and neither was the FE outcome, the difference between the predicted Young's moduli according to the analytical model and the FE model was fixed. The FEM solution was 2% lower than the analytical result for models with cube unit cells and a fixed radius of 0.01 mm and was 60% lower for models with a fixed radius of 0.25 mm. When the cube models had prismatic struts, the FEM solution was 1% higher than the analytical result for fixed edge length 0.01 mm and 21% higher when the fixed edge length was 0.25 mm. The Poisson's ratio in both types of cube models was zero, as expected from the parametric study and as predicted with the analytical model.

The stiffness of the other unit cell geometries was influenced by the size of the model. The difference between the FEM solution and the analytical solution of the Young's modulus in models with truncated octahedron unit cells was less than 5% for when the fixed radius was 0.01 mm and the model size was between 7 and 20 unit cells. When the size was fixed and the radius varied, the difference between the analytical predicated Young's modulus and the FE result was less than 4% when the radius was 0.1 mm or less. The Poisson's ratio fluctuated slightly, but the difference stayed under 15% for all models.

The Young's modulus in two orthogonal directions was obtained for the FE models with rhombic dodecahedron unit cells. In the first direction, the FEM solution of the largest model (12 unit cells) with a strut radius of 0.01 mm was 7% higher than the analytical solution. In the third direction, the FEM solution of the largest model (12 unit cells) with a strut radius of 0.01 mm was 2% higher than the analytical solution. The Young's moduli in both directions converged to a value below the analytical solutions in models with a strut radius of 0.25 mm. This was also observed for the Poisson's ratios. When the number of unit cells was fixed and the radius varied, the FE prediction of the Young's moduli differed less than 9% with the analytical solutions for models with a strut radius of 0.1 mm or less.

3.3. COMPARISON WITH EXPERIMENTAL RESULTS

Although the input parameters for the FE models were the same as for the experimental samples, they resulted into different apparent densities for each geometry. The relation between the AD and the Young's modulus was compared within the FEM data and within the experimental data. Therefore, a trendline was plotted through the experimental data and the offset of the FEM data from this line was evaluated. Each FE model was regenerated ten times. The error bars in the plots indicate the SD of the mechanical property of the Y-axis.

Cube

Based on the experimental data from Parthasarathy *et al.* [18] on cube unit cells with prismatic struts, it was shown that the corresponding FEM data predicted the stiffness of the structure better than the analytical model of Gent and Thomas [24]. However, the SD of the edge length of the struts was higher in the FE models than the SD according to the experimental data. In Figure 9, the Young's modulus as a function of the AD is displayed for four different datasets: Experimental, analytical (with 15% void in the struts), FEM data with the maximum SD of the edge length (based on a minimal printable edge of 0.1 mm) and FEM data with the SD as reported in the experiments. As seen in Figure 7a, the FE models with fixed edge length were stiffer than the corresponding analytical solutions. Since the experimental SD was much smaller than the maximum SD, the resulting stiffness of these models is closer to the stiffness of models with fixed edge length, and like the models with fixed edge length, stiffer than the analytical solution. Trendlines are plotted through the different datasets. The trendline that was used for the analysis of the offset, had the following linear equation:

$$\text{Trendline Parthasarathy: } \mathrm{E} = 6.42\mathrm{AD}$$

The comparison of the datasets can be found in Table 5.1. The main reason that caused the FE models to be stiffer than the experimental samples is the perfectly axial alignment of the cylindrical sections of the beams. In

reality, the sections are not axially aligned, which makes the beams weaker. Neither are the unit cells perfectly cubic shaped. In addition, the sections are in reality not cylindrical, but spherical due to shape of the particles. These differences are visualized in Figure 10.

Diamond

The FE models with diamond unit cells and a Gaussian distribution of the strut radius have proven to especially predict experimental results for small apparent densities. Figure 11 shows the Young's modulus for both datasets as a function of the AD. The trendline through the experimental data of Heinl *et al.* had the following exponential equation:

$$\text{Trendline Heinl: } \mathrm{E} = 81.14\mathrm{AD}^{2.59}$$

The comparison of both datasets is presented in Table 5.2. Because no analytical model of diamond unit cells was available, no comparison could be made between the predication of mechanical properties by FE models or analytical models. However, it can be stated that the FE model predicted the Young's modulus of the titanium foam samples presented by Heinl *et al.* [19] up to 33% accurate for low apparent densities (0.11<AD<0.27).

Rhombic Dodecahedron

In Figure 12, the different datasets of models with rhombic dodecahedron unit cells are plotted. The following trendline through the experimental data of LayerWise was used for the comparison between the FEM data and the analytical data based on the model of Babaee *et al.* [20]:

$$\text{Trendline LayerWise: } \mathrm{E} = 56.43\mathrm{AD}^{2.51}$$

The comparison is listed in Table 5.3. When the AD of the models was smaller than 0.28, the experimental results were closer to the FEM results than to the analytical solution. The FE model predicts the Young's modulus of the experimental samples of LayerWise up to 27% accurate for low apparent densities ($0.15 \leq AD \leq 0.24$). The experimental samples with an AD larger than 0.23 were stiffer than the corresponding FE models.

4. DISCUSSION

In the last paragraph, the focus was on the relation between the AD and the Young's modulus. And although the geometric properties of the FE models were similar to those of the experimental samples, the apparent densities were significantly different. The main manufacturing imperfection that was taken into account was the variation of the radius of the cross-section of the struts. However, the different sections of the struts with

varying radius are modelled as perfectly axial aligned cylindrical segments. In reality, the segments are not cylindrical, but spherical, neither are they perfectly aligned. These differences cause the area between attached strut segments to be smaller in the specimens. As a result the foams are weaker than the FE models. The fact that strut segments are modelled as cylinders with the cross-section radius equal to the radius of the spheres will cause the FE models to contain more material, leading to a higher AD and stiffer models.

Another aspect that can influence the difference in stiffness between the experimental results and FE models is the fact that the bulk structure of the FE models is limited to a cubic shape and can only contain complete unit cells. The models with rhombic dodecahedron unit cells were compared to data from LayerWise that was from cylindrical foam samples. The unit cells in the foam samples with diamond and rhombic dodecahedron cells were cut at the boundaries in order to keep constant sample dimensions, while varying microstructure parameters. The stiffness predication of models from the rhombic dodecahedron unit cell was the least accurate. Therefore, the effects of the sample shape and complete versus cut unit cells on the stiffness of the structure should be studied. The weak mechanical response of the FE models with rhombic dodecahedron unit cells might also be explained by the fact that some of the dimensions of the models were smaller than the size required for a stable stiffness prediction according to the convergence study. However, the corresponding experimental samples had similar dimensions, which were also smaller than the required size and should therefore have a reduced stiffness as well. Furthermore, the effect of the boundary conditions on the mechanical properties should be investigated more thoroughly. As stated by Li *et al.,* displacement boundary conditions that only restrain normal displacements may underestimate foam properties [22, 28].

The results of Parthasarthy *et al.* showed that the mechanical properties are not only dependant on the AD, but also on the cross-section of the struts, its length and the ratio between these two parameters. The fourth sample set of Parthasarathy had a larger offset compared to the other three sets, because the models in the fourth set had short, thin beams as opposed to long, thick beams. In the analytical model of Gent and Thomas, the ratio of edge length to beam length (β) was the input for the Young's modulus calculation [24]. The parameter β is the same in the fourth sample set as in the second sample set, resulting in equal Young's moduli predictions. However, the fact that the beams are short and thin versus long and thick, does result in different apparent densities.

The current study has shown that finite element modeling is a suitable method to predict the stiffness of metal foams. However, the prediction was especially accurate for foams with a low AD. In order to improve the

prediction, more manufacturing effects have to be taken into account. For SEBM, the variations in beam current, scan rate and process temperature can influence the microstructure and mechanical properties of the end product [29]. Simone and Gibson found the melting of the particles and subsequently cooling to cause local heterogeneities and stress concentrations [18, 30]. These effects result into early failure of the thinner struts and therefore, a lower stiffness of the entire structure [18]. However, as mentioned by Parthasarathy *et al.,* studies on SEBM show no differentiation between the printing layers, indicating complete melting of the powder and metallurgical bonding between the layers [18]. Another effect of the manufacturing process is the possible porosity within the struts. In the literature that was used in the current study, this was only observed in the samples with cube unit cells and prismatic struts. Determination of the void percentage in Figure 5a reached a minimum of 9% and maximum of 25%, depending on the grey value set as void. The porosity was assumed to be caused by the square cross-section of the beams.

With FE modeling, metal foams can be designed with the required mechanical and geometric properties. For hip implants, the stiffness optimization will lead to reduced stress shielding and the geometric optimization to reduced micro-motions. Koudelka reported that an open-pore structure with mean pore dimensions of 200-500 µm is susceptible of transport of body fluids and also of ingrowth of new bone tissue [31]. Such pore sizes can be realized with 3D printing. Kuiper and Huiskes modelled a nonhomogeneous stem and optimized its material properties, based on the interface stress distribution and bone resorption [32]. The optimization resulted in a wide ranged Young's modulus that decreased in the distal area, so moving away from the joint. The modulus varied from 16.7 to 100 GPa, with 100 GPa set as upper bound and 20 GPa as modulus of bone. As an example, based on the continuation of the trendline through the experimental data of the samples with diamond unit cells, a Young's modulus of 16.7 GPa can be realized by generating titanium foam with diamond unit cells and an AD of 0.54.

5. FUTURE WORK AND RECOMMENDATIONS

The main recommendation for the FE modeling tool is to include the option to randomly align the beam segments. This will most likely improve the accuracy of the stiffness prediction of 3D printed metal foams. Future applications of the modeling tool and FEM in general can be within the design process of a wide variation of products. By formulating objective functions, mechanical and geometrical properties can be optimized (e.g. for an artificial hip such functions can be minimizing interface shear stresses or minimizing resorbed bone). Before the metal foams are used for biomedical applications, they should be tested on fatigue

behaviour, reaction to a humid environment and influence of temperature on their mechanical properties. In addition, the surface response of the surrounding tissue at the foam/tissue interface needs to be tested.

6. CONCLUSION

The main conclusion of this study is that finite element modeling can be used for prediction of bulk mechanical properties of 3D printed titanium foams. The irregular geometry of the foam's microstructure can be approached in FE models with a Gaussian distribution of the radius or edge length of the cross-section of the struts. By assigning a void percentage to the matrix material, porosity within the struts caused by manufacturing imperfections can be modelled. It was shown that models generated with a specially developed modeling tool approached the mechanical response of foam samples with similar geometrical properties. In order to improve the accuracy of the stiffness prediction, especially for foams with higher apparent densities, more imperfections in the microstructure as a consequence of the manufacturing technique have to be included. Further development is required, but FE modeling has shown to be a promising method to predict the bulk mechanical properties of 3D printed metal foams.

7. ACKNOWLEDGEMENT

I would like to thank the people on my graduation committee for their time, effort and professional feedback during the project: Prof.dr.ir. Harrie Weinans, assistant professor Dr. Amir Zadpoor, PhD candidate Gianni Campoli and Ir. Jos Sinke. My daily contact was with Gianni and Amir and therefore, I would like to especially thank them. They were always available for questions or discussion, and really helped me to come to this result. Lastly, I would like to thank LayerWise for sharing their data with us from the compression tests on the rhombic dodecahedron samples.

8. APPENDIX

8.1. ANALYTICAL MODELS

Gent and Thomas [24] formulated an analytical model for the stiffness of open cellular solids with cubic unit cells and prismatic struts. The parameter β was defined by the ratio of the square side and the strut length, but could also be derived through the AD. The cube models generated with the GUI can have cylindrical beams or prismatic beams. The model of Gent and Thomas suited both geometries, but for the prismatic beams an even simpler version of the model satisfied. This model fitted an infinite tessellated cellular structure. Therefore, β was determined for an infinite structure and consequently, the analytical solution of the Young's modulus was as well.

Roberts and Garboczi [25] derived an analytical model for the stiffness of the truncated octahedron that also fitted an infinite tessellated structure. They referred for their analytical expressions to previously formulated models by Zhu et al. (1997) and Warren and Kraynik (1997) [25, 33, 34].

Babaee *et al.* [20] derived analytical expressions for the Young's modulus and Poisson's ratio of a single rhombic dodecahedron and infinitely tessellated rhombic dodecahedrons. The analytical model was based on low apparent densities, where bending of the edges is the dominant deformation mechanism. Because of the shape of the unit cell, the structure has orthotropic mechanical properties. The coordinate system that was used in the paper of Babaee, was different from our coordinate system (their 1st = our 3rd direction, their 2nd = our 2nd and their 3rd = our 1st), but that is already adjusted in the formulas presented. The mechanical properties in the second and third direction were equal due to symmetry. Furthermore, the unit cells in Babaee's model were composed of prismatic beams instead of cylindrical beams. Therefore, based on their derivations, the analytical expressions for cylindrical beams were derived. The Young's moduli found in FE models with fixed radius should eventually converge to the analytically derived moduli. By increasing the size of the FE model, the variation was expected to decrease, because the definition of the strain energy function was based on an infinite tessellated structure.

The starting point of the analytical model was the strain energy held by the struts in the direction of the loading. In the first direction, the loading is divided over six strut segments, each containing two struts. In the second or third direction, the loading is experienced by a strut segment that contains four struts. Figure 17 shows the loading in both directions.

Young's modulus in 1st direction

$$Loading\ is\ divided\ over\ 6\ strut\ segments\colon P = \frac{F_1}{6}$$

$$From\ the\ free\ body\ diagram\ of\ one\ strut\ in\ \textbf{Figure 17}\colon\ M = \frac{PL\cos\theta}{2}$$

$$Ignoring\ the\ shear\ strain\ energy, gives\colon$$

$$U_1 = 6\int_0^L \frac{M^2}{2E_sI}dx_s + 6\int_0^L \frac{N^2}{2E_sA}dx_s,$$

$$The\ first\ part\ is\ the\ strain\ energy\ stored\ in\ a\ beam\ subject\ to\ pure\ bending,$$

$$the\ second\ part\ to\ axial\ force.$$

$$Internal\ moment\ M = \frac{PL\cos\theta}{2}, \qquad axial\ force\ N = P\sin\theta$$

$$U_1 = 6\int_0^L \frac{P^2 L^2 \cos^2\theta}{4 \cdot 2E_s I}\,dx_s + 6\int_0^L \frac{P^2 \sin^2\theta}{2E_s A}\,dx_s$$

$$U_1 = 6\int_0^L \frac{{F_1}^2 L^2 \cos^2\theta}{36 \cdot 4 \cdot 2E_s I}\,dx_s + 6\int_0^L \frac{{F_1}^2 \sin^2\theta}{36 \cdot 2E_s A}\,dx_s$$

$$\textit{Application of the Castigliano's second theorem: } \frac{\partial U_1}{\partial F_1} = \delta_{11}$$

$$\frac{\partial U_1}{\partial F_1} = 6\int_0^L \frac{F_1 L^2 \cos^2\theta}{144E_s I}\,dx_s + 6\int_0^L \frac{F_1 \sin^2\theta}{36E_s A}\,dx_s$$

$$\frac{\partial U_1}{\partial F_1} = \left[\frac{F_1 L^3 \cos^2\theta}{24E_s I}\right] + \left[\frac{F_1 L \sin^2\theta}{6E_s A}\right],$$

$$24 \textit{ should be } 72, \textit{ because that is required to come to the correct final expression}$$

$$\delta_{11} = \frac{PL^3 \cos^2\theta}{12E_s I} + \frac{PL \sin^2\theta}{E_s A},$$

$$\textit{where } A = \pi r^2 \textit{ is the area of the beam cross} - \textit{section and } \theta = 54.73°$$

$$\varepsilon_{11} = \frac{\delta_{11}}{L \sin\theta}, \qquad \sigma_1 = \frac{F_1}{A_{eff}}, \qquad A_{eff} = 4L^2 \sin 2\theta$$

$$\textit{Elastic modulus of one unit cell: } E_1^u = \frac{\sigma_1}{\varepsilon_{11}}$$

$$\frac{E_1^u}{E_s} = \frac{\frac{\sin\theta}{4\sin 2\theta}}{\left(\frac{L^4 \cos^2\theta}{72I} + \frac{L^2 \sin^2\theta}{6A}\right)}, \qquad \cos^2 54.73° \approx \frac{1}{3}, \sin^2 54.73° \approx \frac{2}{3}$$

$$\frac{E_1^u}{E_s} = \frac{\frac{54\sin\theta}{\sin 2\theta}}{\frac{L^4}{I} + \frac{24L^2}{A}}$$

$$= \frac{\frac{54\sin\theta}{\sin 2\theta}}{\frac{4L^4}{\pi r^4} + \frac{24L^2}{\pi r^2}}$$

$$= \frac{\frac{27\sin\theta}{\sin 2\theta}}{\frac{2L^4}{\pi r^4} + \frac{12L^2}{\pi r^2}}$$

$$\textit{Babaee states the modulus of the unit cell to be } \frac{3}{2} \textit{ of the whole: } E_1^u \frac{2}{3} = E_1$$

$$\frac{E_1}{E_s} = \frac{\frac{27\sin\theta}{\sin 2\theta}}{\frac{3L^4}{\pi r^4} + \frac{18L^2}{\pi r^2}}, \qquad \theta = 54.73°$$

Young's modulus in 3rd direction

To calculate the Young's modulus in the third direction, again the strain energy in the strut segment was the basis.

$$Loading\ is\ divided\ over\ 4\ struts\colon C = \frac{F_3}{4}$$

$$U_3 = 4\int_0^L \frac{M^{*2}}{2E_sI}dx_s + 4\int_0^L \frac{N^{*2}}{2E_sA}dx_s$$

$$C = \frac{F_3}{4} = \frac{\sigma_3 A_3}{4}, where\ A_3 = 4L^2\sin^2\theta\ is\ the\ effective\ CS\ area\ in\ direction\ 3\ and\ \theta = 54.73°$$

$$M^* = -M + \frac{\sqrt{2}Cx_s}{2\sqrt{3}}, N^* = -\frac{C}{\sqrt{3}}$$

$$Minimizing\ total\ stain\ energy\ with\ respect\ to\ M\colon$$

$$U_3 = 4\int_0^L \frac{M^2 - \frac{\sqrt{2}}{\sqrt{3}}MCx_s + \frac{1}{6}C^2x_s^2}{2E_sI}dx_s + 4\int_0^L \frac{N^{*2}}{2E_sA}dx_s$$

$$\frac{\partial U_3}{\partial M} = 4\int_0^L \frac{2M - \frac{\sqrt{2}}{\sqrt{3}}Cx_s}{2E_sI}dx_s$$

$$\frac{\partial U_3}{\partial M} = 0\ for\ M = \frac{\sqrt{2}Cx_s}{2\sqrt{3}}$$

$$Application\ of\ Castigliano's\ second\ theorem\colon \frac{\partial U_3}{\partial F_3} = \delta_{33}$$

$$U_3 = 4\int_0^L \frac{F_3^2x_s^2}{96E_sI}dx_s + 4\int_0^L \frac{F_3^2}{96E_sA}dx_s$$

$$Ignoring\ the\ strain\ energy\ associated\ with\ shear\ and\ axial\ deformation\colon$$

$$\frac{\partial U_3}{\partial F_3} = 4\int_0^L \frac{2F_3x_s^2}{96E_sI}dx_s$$

$$\delta_{33} = 4\left[\frac{2F_3x_s^3}{288E_sI}\right]_0^L$$

$$= \frac{F_3L^3}{36E_sI}$$

$$= \frac{CL^3}{9E_sI}$$

$$E_3 = \frac{\sigma_3}{\varepsilon_{33}}, \quad \varepsilon_{33} = \frac{\delta_{33}}{2L\cos\theta}, \quad \delta_{33} = \frac{CL^3}{9E_sI}, \quad C = \frac{F_3}{4} = \frac{\sigma_3A_3}{4}, \quad where\ A_3 = 4L^2\sin^2\theta$$

$$\frac{E_3}{E_s} = \frac{18I\cos\theta}{L^4\sin^2\theta}$$

$$Conclusion: \qquad \frac{E_1}{E_s} = \frac{\frac{27\sin\theta}{\sin 2\theta}}{\frac{3L^4}{\pi r^4} + \frac{18L^2}{\pi r^2}}, \qquad \frac{E_3}{E_s} = \frac{9\pi r^4\cos\theta}{2L^4\sin^2\theta}, \qquad \theta = 54.73°$$

8.2. CORRECTION APPARENT DENSITY IN FE MODELS

In the FEM data, the AD was overestimated because intersecting beam-ends were double-counted. This needed to be corrected when comparing the FEM data of models with a Gaussian distributed strut radius to experimental data. In this comparison, the relation between the Young's modulus and the AD was analyzed. The correct AD was required to properly compare these two relations. Therefore, FE models of the intersections were generated and the double-counted volume was obtained. Different models were made of different type of intersections for each geometry. First the foam volume according to the FEM data *(V_{foam} FEM)* was attained by dividing the volume of the total structure *(X·Y·Z)* by the AD according to the FEM data *(AD FEM).* The models of the intersections told us the double-counted volume *(DC V_{joint})*. Hand calculations or FE modeling was used to determine the number of joints per geometry and per type of intersection (*Jn,* with *n* the number of struts intersecting). Multiplication of the number of joints by the double-counted volume per joint resulted in the total double-counted volume *(DC V_{tot}).* Wherefrom the correct volume of the foam *(V_{foam} Real)* could be calculated, leading to the real apparent density *(AD Real).*

$$\frac{X \cdot Y \cdot Z}{AD\ FEM} = V_{foam}FEM$$

$$DC\ V_{joint} \cdot no.joints = DC\ V_{tot}$$

$$V_{foam}FEM - DC\ V_{tot} = V_{foam}Real$$

$$\frac{V_{foam}Real}{X \cdot Y \cdot Z} = AD\ Real$$

$$UC_i = number\ of\ unit\ cells\ in\ i\ direction$$

Cube

$$No.J3 = 8$$

$$No.J4 = 4(UC_x - 1) + 4\big(UC_y - 1\big) + 4(UC_z - 1)$$

$$No.J5 = (UC_x - 1)\big(UC_y - 1\big) + (UC_x - 1)(UC_z - 1) + \big(UC_y - 1\big)(UC_z - 1)$$

$$No.J6 = (UC_x - 1) \cdot \big(UC_y - 1\big) \cdot (UC_z - 1)$$

Diamond & Rhombic Dodecahedron

For models with diamond and rhombic dodecahedron unit cells, the number of intersections was determined through FE models. Models were generated with only one 2-node element per strut. Within the part a set was created which included all nodes. The following command computed the number of nodes which was shared by *n* elements.

```
x=mdb.models['X_model'].rootAssembly.instances['X_PART-FOAM-1'].sets['All'].nodes
nodes=range(len(x))
node_data= {}
l=[0]*len(x)
for i in nodes:
        l[i]=len(x[i].getElements())
        if l[i]==n:
                node_data[x[i].label]=x[i].getElements()
len(node_data.keys()
```

8.3. ADDITIONAL FIGURES AND TABLES

See Figures captions and Tables captions.

9. REFERENCES

[1] J. M. Elkins, X. C. Liu, X. Qin, Z. Du, and T. D. Brown, "Ceramic Total Hip Liner Fracture Modeling in Abaqus using co-Simulation and Extended Finite Element Modeling," 2011.

[2] J. D'Antonio, W. Capello, M. Manley, and B. Bierbaum, "New experience with alumina-on-alumina ceramic bearings for total hip arthroplasty," *J Arthroplasty,* vol. 17, pp. 390-397, 2002.

[3] P. Söderman, H. Malchau, P. Herberts, R. Zügner, H. Regnér, and G. Garellick, "Outcome after total hip arthroplasty: Part II. Disease-specific follow-up and the Swedish National Total Hip Arthroplasty Register," *Acta Orthop,* vol. 72, pp. 113-119, 2001.

[4] P. Söderman, H. Malchau, and P. Herberts, "Outcome after total hip arthroplasty: Part I. General health evaluation in relation to definition of failure in the Swedish National Total Hip Arthroplasty register," *Acta Orthop,* vol. 71, pp. 354-359, 2000.

[5] M. Sundfeldt, L. V Carlsson, C. B Johansson, P. Thomsen, and C. Gretzer, "Aseptic loosening, not only a question of wear: A review of different theories," *Acta Orthop,* vol. 77, pp. 177-197, 2006.

[6] M. Fraldi, L. Esposito, G. Perrella, A. Cutolo, and S. Cowin, "Topological optimization in hip prosthesis design," *Biomechanics and Modeling in Mechanobiology,* vol. 9, pp. 389-402, 2010.

[7] G. Isaac, J. Thompson, S. Williams, and J. Fisher, "Metal-on-metal bearings surfaces: materials, manufacture, design, optimization, and alternatives," *Proc Inst Mech Eng H,* vol. 220:119, 2006.

[8] P. Steven Kurtz, P. Kevin Ong, M. Edmund Lau, P. Fionna Mowat, and M. Michael Halpern, MD, PhD, "Projections of Primary and Revision Hip and Knee Arthroplasty in the United States from 2005 to 2030," *The Journal of Bone and Joint Surgery,* vol. 89, pp. 780-785, 2007.

[9] P. Herberts and H. Malchau, "Long-term registration has improved the quality of hip replacement: A review of the Swedish THR Register comparing 160,000 cases," *Acta Orthop,* vol. 71, pp. 111-121, 2000.
[10] J. C. Clohisy, G. Calvert, F. Tull, D. McDonald, and W. J. Maloney, "Reasons for Revision Hip Surgery: A Retrospective Review," *Clin Orthop Relat Res,* vol. 429, pp. 188-192, 2004.
[11] H. Bougherara, M. Bureau, M. Campbell, A. Vadean, and L. H. Yahia, "Design of a biomimetic polymer-composite hip prosthesis," *Journal of Biomedical Materials Research Part A,* vol. 82A, pp. 27-40, 2007.
[12] M. G. Joshi, S. G. Advani, F. Miller, and M. H. Santare, "Analysis of a femoral hip prosthesis designed to reduce stress shielding," *Journal of Biomechanics,* vol. 33, pp. 1655-1662, 2000.
[13] L. Fratila, "Class Lecture 2, Biomaterials," TU Delft 2010-2011.
[14] K. R. Berend, A. V. Lombardi Jr, A. F. Ajluni, B. E. Seng, and M. D. Skeels, "Metal-on-metal bearings in primary total hip arthroplasty," 2010.
[15] L. Fratila, "Class Lecture 3, Biomaterials," TU Delft 2010-2011.
[16] P. Soman, J. W. Lee, A. Phadke, S. Varghese, and S. Chen, "Spatial Tuning of Negative and Positive Poisson's ratio in a Multi-layer Scaffold," *Acta Biomaterialia,* 2012.
[17] S. Van Bael, G. Kerckhofs, M. Moesen, G. Pyka, J. Schrooten, and J. P. Kruth, "Micro-CT-based improvement of geometrical and mechanical controllability of selective laser melted Ti6Al4V porous structures," *Materials Science and Engineering: A,* 2011.
[18] J. Parthasarathy, B. Starly, S. Raman, and A. Christensen, "Mechanical evaluation of porous titanium (Ti6Al4V) structures with electron beam melting (EBM)," *Journal of the Mechanical Behavior of Biomedical Materials,* vol. 3, pp. 249-259, 2010.
[19] P. Heinl, C. Körner, and R. F. Singer, "Selective electron beam melting of cellular titanium: Mechanical properties," *Advanced Engineering Materials,* vol. 10, pp. 882-888, 2008.
[20] S. Babaee, B. H. Jahromi, A. Ajdari, H. Nayeb-Hashemi, and A. Vaziri, "Mechanical properties of open-cell rhombic dodecahedron cellular structures," *Acta Materialia,* 2012.
[21] J. R. Barber, *Intermediate Mechanics of Materials*: Springer, 2010.
[22] K. Li, X. L. Gao, and G. Subhash, "Effects of cell shape and strut cross-sectional area variations on the elastic properties of three-dimensional open-cell foams," *Journal of the Mechanics and Physics of Solids,* vol. 54, pp. 783-806, 2006.
[23] M. Van der Burg, V. Shulmeister, E. Van der Geissen, and R. Marissen, "On the linear elastic properties of regular and random open-cell foam models," *Journal of cellular plastics,* vol. 33, pp. 31-54, 1997.
[24] A. Gent and A. Thomas, "Mechanics of foamed elastic materials," *Rubber Chemistry and Technology,* vol. 36, p. 597, 1963.
[25] A. P. Roberts and E. J. Garboczi, "Elastic properties of model random three-dimensional open-cell solids," *Journal of the Mechanics and Physics of Solids,* vol. 50, pp. 33-55, 2002.
[26] Arcam-EBM-System. *Ti-6Al-4V*.
[27] Y. Lee, M. Peters, and G. Welsch, "Elastic moduli and tensile and physical properties of heat-treated and quenched powder metallurgical Ti-6Al-4V alloy," *Metallurgical and Materials Transactions A,* vol. 22, pp. 709-714, 1991.
[28] K. Li, X. L. Gao, and G. Subhash, "Effects of cell shape and cell wall thickness variations on the elastic properties of two-dimensional cellular solids," *International Journal of Solids and Structures,* vol. 42, pp. 1777-1795, 2005.
[29] L. Murr, S. Quinones, S. Gaytan, M. Lopez, A. Rodela, E. Martinez, D. Hernandez, E. Martinez, F. Medina, and R. Wicker, "Microstructure and mechanical behavior of Ti-6Al-4V produced by rapid-layer manufacturing, for biomedical applications," *Journal of the Mechanical Behavior of Biomedical Materials,* vol. 2, pp. 20-32, 2009.
[30] A. Simone and L. Gibson, "The effects of cell face curvature and corrugations on the stiffness and strength of metallic foams," *Acta Materialia,* vol. 46, pp. 3929-3935, 1998.
[31] P. Koudelka, O. Jiroušek, T. Doktor, P. Zlámal, and T. Fıla, "COMPARATIVE STUDY ON NUMERICAL AND ANALYTICAL ASSESSMENT OF ELASTIC PROPERTIES OF METAL FOAMS," *Structure,* vol. 1, p. 1.37, 2012.
[32] J. H. H. Kuiper, R., "Mathematical Optimization of Elastic Properties: Application to Cementless Hip Stem Design," *Journal of Biomechanical Engineering,* vol. 119, pp. 166-174, May 1997 1997.
[33] W. Warren and A. Kraynik, "Linear elastic behavior of a low-density Kelvin foam with open cells," *Journal of applied mechanics,* vol. 64, p. 787, 1997.
[34] H. Zhu, J. Knott, and N. Mills, "Analysis of the elastic properties of open-cell foams with tetrakaidecahedral cells," *Journal of the Mechanics and Physics of Solids,* vol. 45, pp. 319-343, 1997.

FIGURE CAPTIONS

Figure 1. Component generation layer by layer with SEBM, adopted from Heinl *et al.* [19]

Figure 2. The developed graphical user interface (three different tabs) to generate metal foams in Abaqus

Figure 3. The geometries of the different unit cells

Figure 4. Flow chart of the method

Figure 5. SEM images of the cross-section of different struts: (a) prismatic strut of a cubic unit cell, adopted from Parthasarathy *et al.* [18], (b) cylindrical strut of a diamond unit cell, adopted from Heinl *et al.* [19] and (c) cylindrical strut of a rhombic dodecahedron unit cell, taken with the scanning electron microscope at TU Delft

Figure 6. Gaussian distribution of the cross-section size of the strut

Figure 7. Comparison FEM data with analytical data: Young's modulus as a function of the number of unit cells in models with strut radius 0.25 mm for geometries (a) cube, (b) diamond, truncated octahedron and rhombic dodecahedron; Poisson's ratio as a function of the strut radius in models with 10 unit cells for geometries (c) cube and truncated octahedron, (d) diamond and rhombic dodecahedron; Young's modulus as a function of the strut radius in models with 10 unit cells for (e) all four geometries;

Figure 8. Young's modulus as a function of the standard deviation of the mean radius in models with 10 unit cells and mean strut radius 0.25 mm for geometries (a) cube and rhombic dodecahedron, (b) diamond and truncated octahedron (n=10); Poisson's ratio as a function of the standard deviation of the mean radius in models with 10 unit cells and mean strut radius 0.25 mm for geometries (c) cube and diamond, (d) truncated octahedron and rhombic dodecahedron (n=10)

Figure 9. Comparison Young's modulus as a function of the apparent density between cubic models with prismatic beams: Parthasarathy's data (Experimental), analytical data based on Gent and Thomas' model with 15% fixed porosity (Analytical) and FEM data of models with 10-20% porosity within the beams (SD 0.025) and a Gaussian distributed edge length with two different standard deviations, maximum SD based on minimum printable edge length 0.1 mm (FEM SD Max.) and SD as reported by Parthasarathy (FEM SD Exp.)

Figure 10. Axial alignment beam segments, (a) FEM and (b) Additive manufactured

Figure 11. Comparison Young's modulus as a function of the apparent density between Heinl's data (Experimental) and FEM data (FEM) of diamond unit cells with a Gaussian distribution of the cross-section radius (ratio SD to mean radius is 1:6, based on the measured ratio in Figure 5c)

Figure 12. Comparison Young's modulus as a function of the apparent density between data from LayerWise (Experimental), analytical data based on Babaee's model (Analytical) and FEM data (FEM) of rhombic dodecahedron unit cells with a Gaussian distribution of the cross-section radius (SD based on the measured ratio between SD and mean radius in Figure 5c)

APPENDIX 8.3.1.

Figure 13. Comparison FEM data with analytical data: Young's modulus as a function of the number of unit cells in models with strut radius 0.01 mm for (a) cube, (b) truncated octahedron and rhombic dodecahedron

Figure 14. Poisson's ratio as a function of the number of unit cells in models with fixed radius/edge 0.25 mm for (a) cube and truncated octahedron, (b) diamond and rhombic dodecahedron

Figure 15. Young's modulus as a function of the number of unit cells in models with a Gaussian distribution of the radius, mean radius 0.25 mm with SD 0.02 mm for (a) cube, (b) diamond, truncated octahedron and rhombic dodecahedron (n=10)

Figure 16. Poisson's ratio as a function of the number of unit cells in models with a Gaussian distribution of the radius, mean radius 0.25 mm with SD 0.02 mm for (a) cube, (b) diamond, (c) truncated octahedron and (d) rhombic dodecahedron (n=10)

Figure 17. Loading of rhombic dodecahedron in first (a) and second direction (b) with adjusted coordinate system to our coordinate system, adopted from Babaee *et al.* [20]

TABLE CAPTIONS

Table 1. Standard input parameters FEM

Table 2. Input parameters and experimental results on 3D printed Ti-6Al-4V foams, (a) cube samples from Parthasarathy *et al.* (2010) [18], (b) diamond samples from Heinl *et al*. (2008) [19] and (c) rhombic dodecahedron samples from LayerWise

Table 3. Comparison apparent density according to FEM and according to hand calculations

Table 4. Number of unit cells required for a stable, predictable stiffness; Based on the assumption that the structure is considered stable when an extra unit cell (UC+1) changes the predicted property by less than 1, 5 or 10%

Table 5. Comparison (c) experimental results from Table 2 with FEM data (a) and analytical data (b), 1) cube, 2) diamond, 3) rhombic dodecahedron

APPENDIX 8.3.2.

Table 6. Young's modulus as a function of the number of unit cells in models with a Gaussian distribution of the radius, mean radius 0.25 mm and SD 0.02 mm, (a) cube, (b) diamond, (c) truncated octahedron and (d) rhombic dodecahedron, standard deviation in parentheses (n=10)

Table 7. Young's modulus as a function of the standard deviation of the mean radius in models with 10 unit cells and mean strut radius 0.25 mm, (a) cube, (b) diamond, (c) truncated octahedron and (d) rhombic dodecahedron, standard deviation in parentheses (n=10)

Table 8. Comparison FEM data with analytical model of Gent and Thomas [24] for cube unit cells with prismatic struts, (a) increasing unit cells with fixed edge length 0.01 mm, (b) increasing unit cells with fixed edge length 0.25 mm, (c) increasing edge length for models with fixed size 10 unit cells

Table 9. Comparison FEM data with analytical model of Gent and Thomas [24] for cube unit cells with cylindrical struts, (a) increasing unit cells with fixed radius 0.01 mm, (b) increasing unit cells with fixed radius 0.25 mm, (c) increasing radius for models with fixed size 10 unit cells

Table 10. FEM data on models with diamond unit cells, (a) increasing unit cells with fixed radius 0.01 mm, (b) increasing unit cells with fixed radius 0.25 mm, (c) increasing radius for models with fixed size 10 unit cells

Table 11. Comparison FEM data with analytical model of Roberts and Garboczi [25] for truncated octahedron unit cells, (a) increasing unit cells with fixed radius 0.01 mm, (b) increasing unit cells with fixed radius 0.25 mm, (c) increasing radius for models with fixed size 10 unit cells

Table 12. Comparison FEM data with analytical model of Babaee *et al.* [20] for rhombic dodecahedron unit cells, (a) increasing unit cells with fixed radius 0.01 mm and compression in direction [1,0,0], (b) increasing unit cells with fixed radius 0.25 mm and compression in direction [1,0,0], (c) increasing unit cells with fixed radius 0.01 mm and compression in direction [0,0,1], (d) increasing unit cells with fixed radius 0.25 mm and compression in direction [0,0,1], (e) increasing radius for models with fixed size 10 unit cells and compression in direction [1,0,0], (f) increasing radius for models with fixed size 10 unit cells and compression in direction [0,0,1]

Figure 1

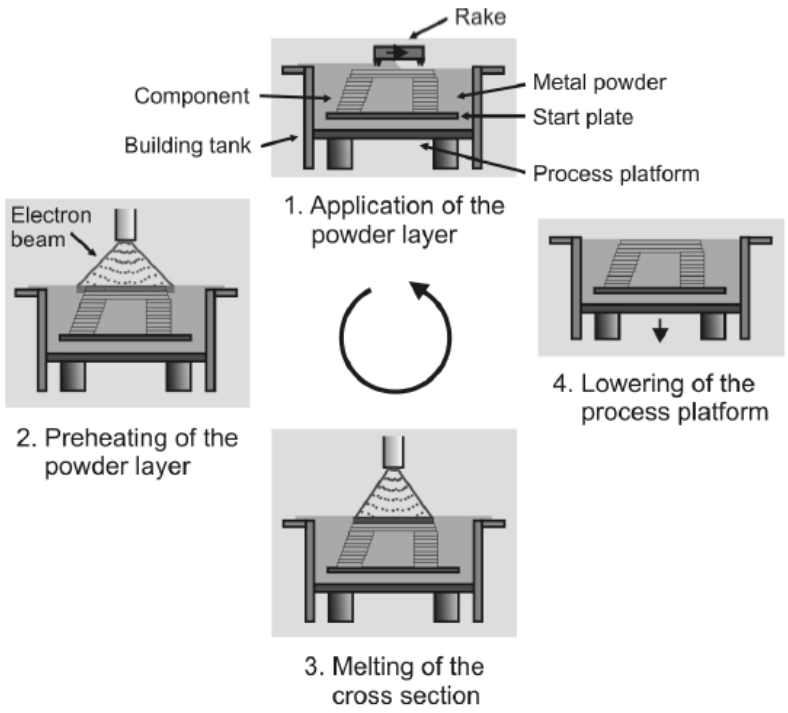
Rake
Component
Building tank
Metal powder
Start plate
Process platform
1. Application of the powder layer
Electron beam
2. Preheating of the powder layer
3. Melting of the cross section
4. Lowering of the process platform

Figure 2

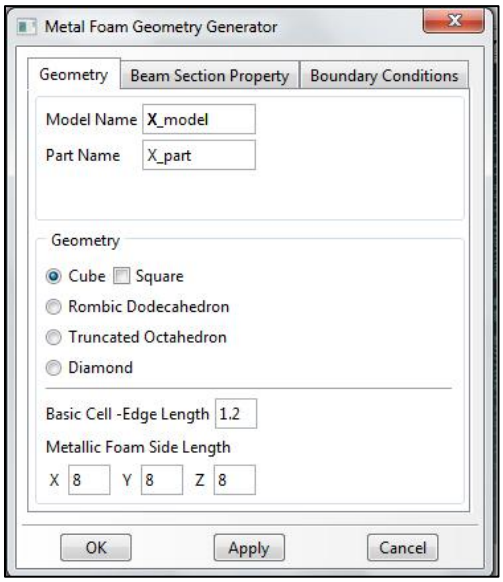
Metal Foam Geometry Generator
Geometry
Beam Section Property
Boundary Conditions
Model Name X_model
Part Name X_part
Geometry
Cube
Square
Rombic Dodecahedron
Truncated Octahedron
Diamond
Basic Cell -Edge Length 1.2
Metallic Foam Side Length
X 8 Y 8 Z 8
OK
Apply
Cancel

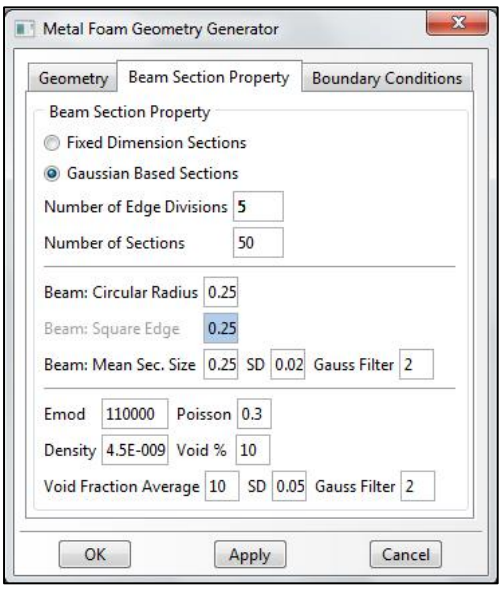
Metal Foam Geometry Generator
Geometry
Beam Section Property
Boundary Conditions
Beam Section Property
Fixed Dimension Sections
Gaussian Based Sections
Number of Edge Divisions 5
Number of Sections 50
Beam: Circular Radius 0.25
Beam: Square Edge 0.25
Beam: Mean Sec. Size 0.25 SD 0.02 Gauss Filter 2
Emod 110000 Poisson 0.3
Density 4.5E-009 Void % 10
Void Fraction Average 10 SD 0.05 Gauss Filter 2
OK
Apply
Cancel

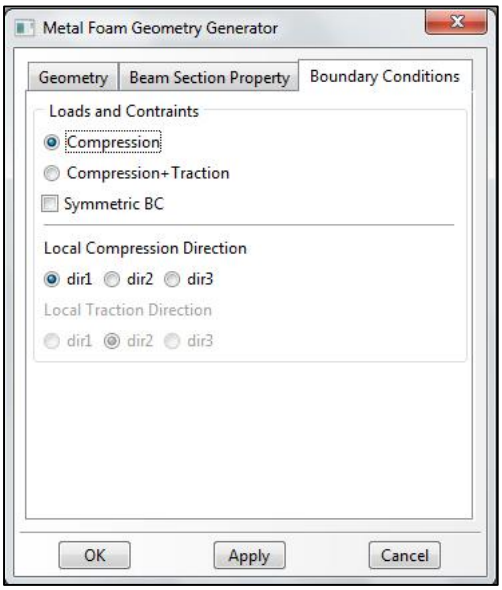
Metal Foam Geometry Generator
Geometry
Beam Section Property
Boundary Conditions
Loads and Contraints
Compression
Compression+Traction
Symmetric BC
Local Compression Direction
dir1 dir2 dir3
Local Traction Direction
dir1 dir2 dir3
OK
Apply
Cancel

Figure 3

Cube

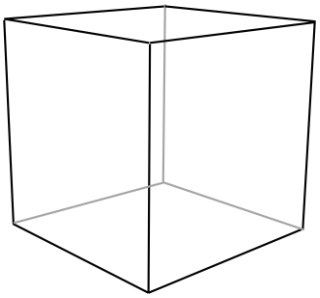

Diamond

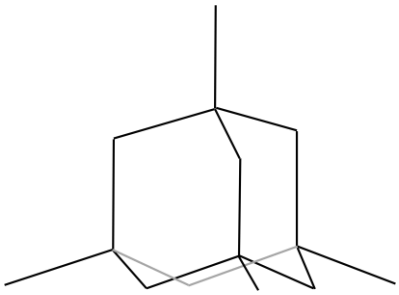

Truncated Octahedron

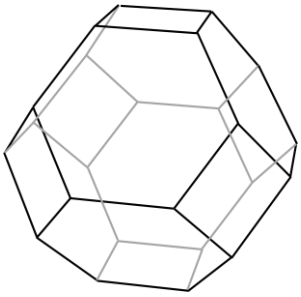

Rhombic Dodecahedron

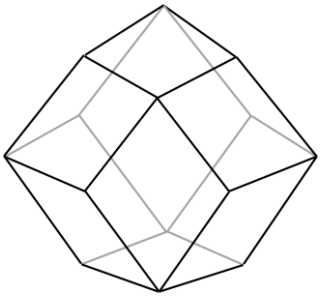

Figure 4

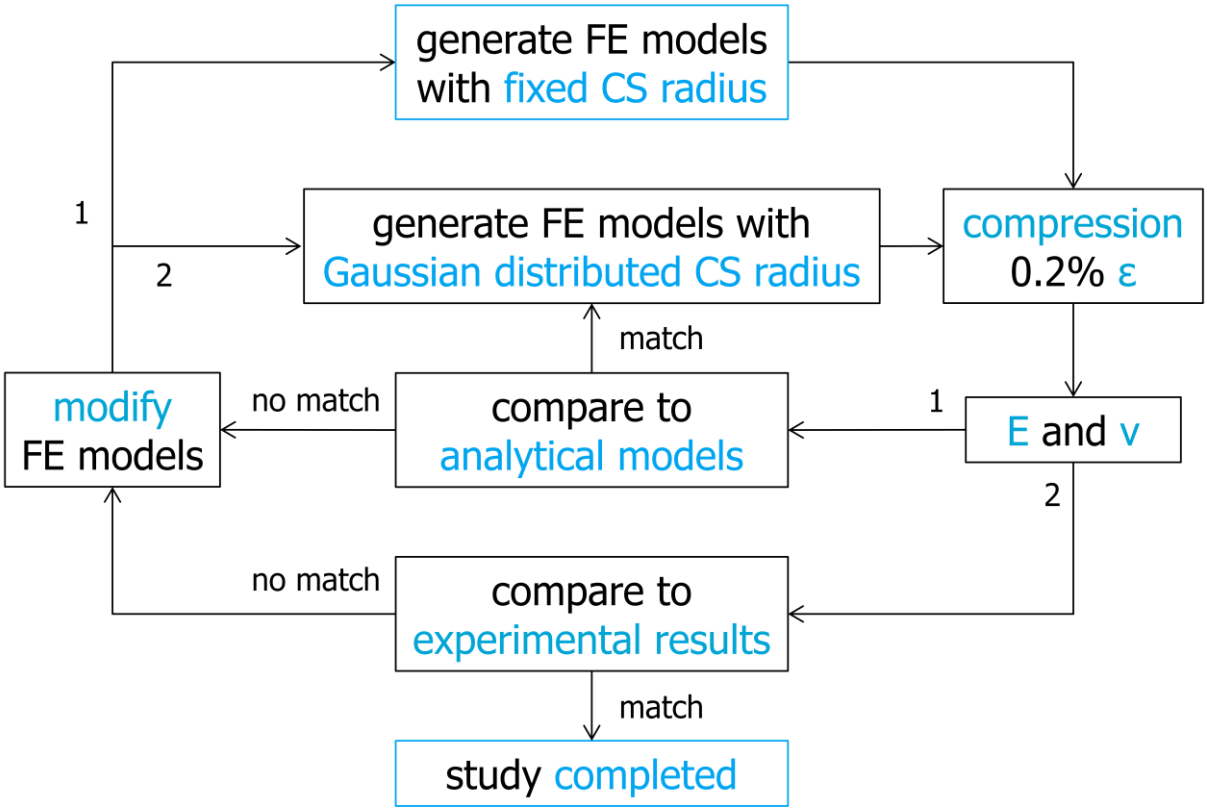
generate FE models with fixed CS radius
1
2
generate FE models with Gaussian distributed CS radius
compression 0.2% ε
match
modify FE models
no match
compare to analytical models
1
E and ν
2
no match
compare to experimental results
match
study completed

Figure 5

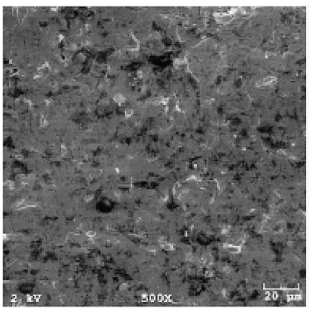
2 kV
500x
20 µm

a)

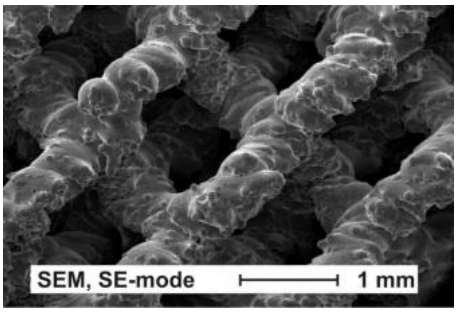
SEM, SE-mode
1 mm

b)

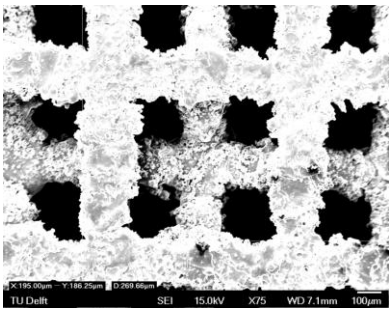
TU Delft
SEI
15.0kV
X75
WD 7.1mm
100µm

c)

Figure 6

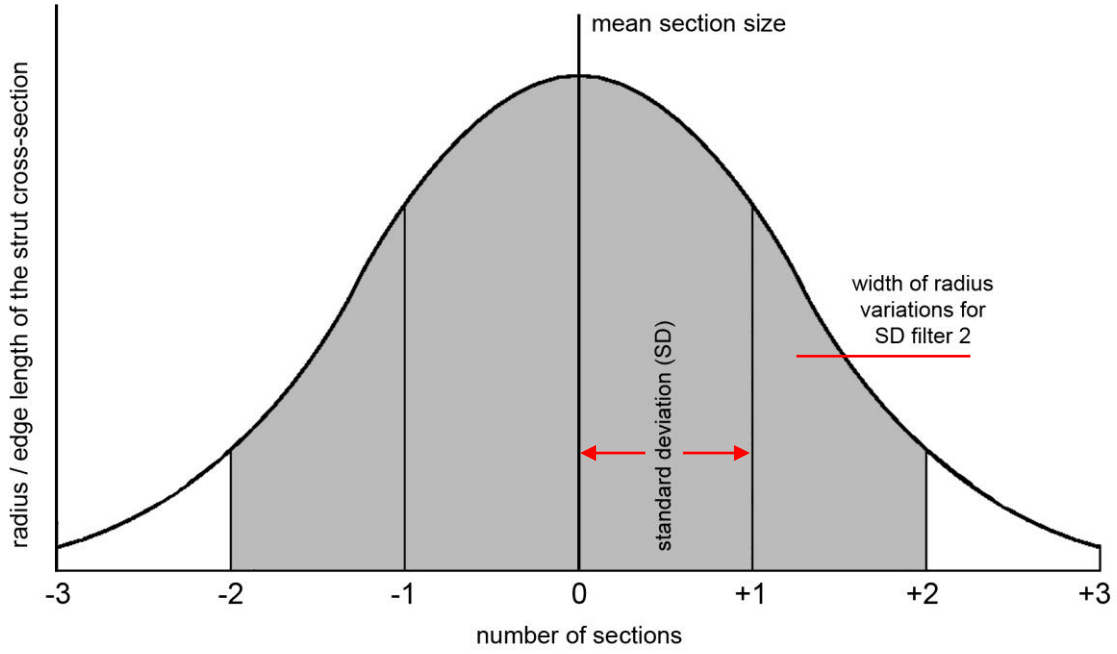
mean section size
radius / edge length of the strut cross-section
width of radius
variations for
SD filter 2
standard deviation (SD)
-3
-2
-1
0
+1
+2
+3
number of sections

Figure 7

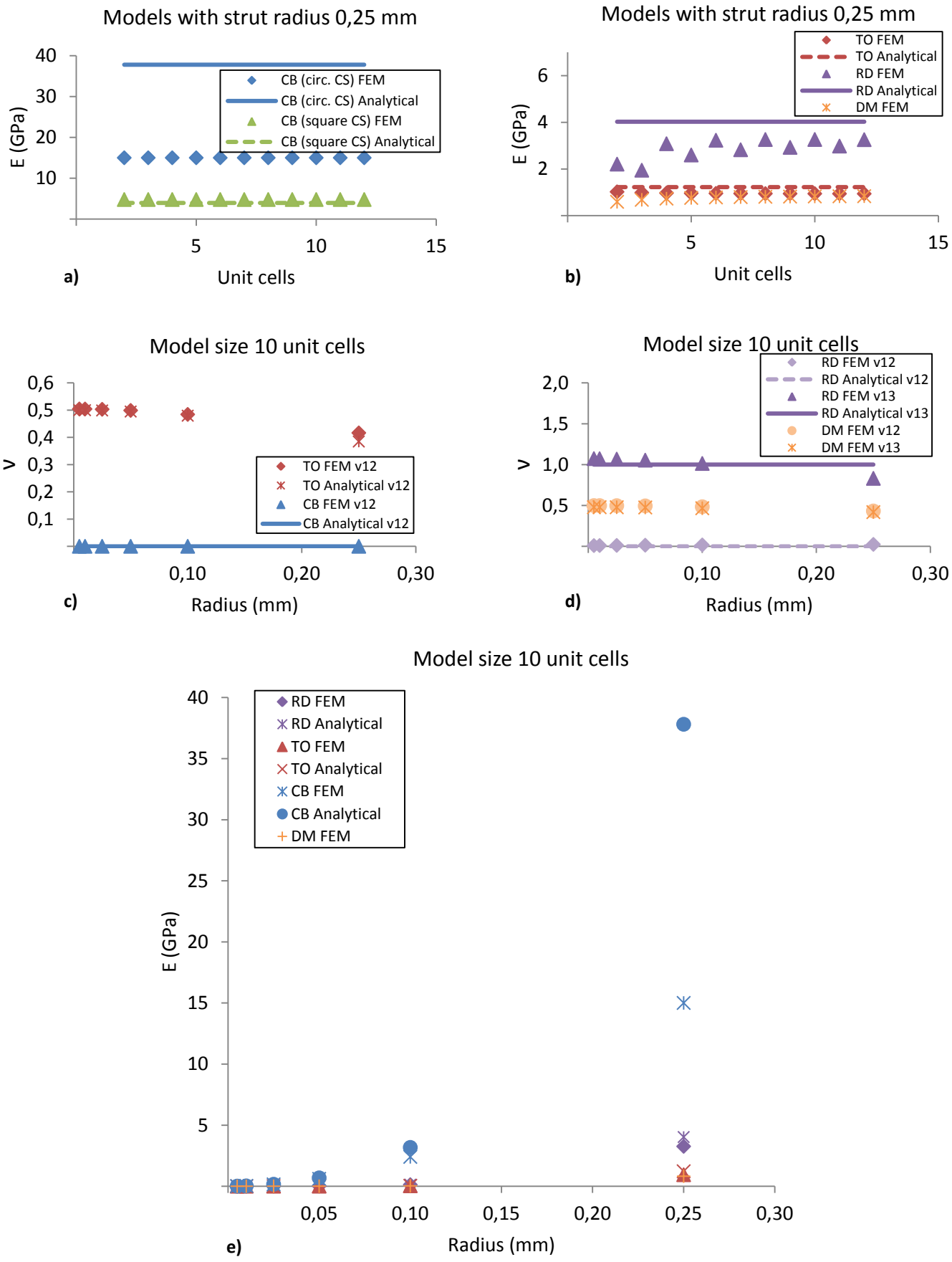
Models with strut radius 0,25 mm
E (GPa)
Unit cells
CB (circ. CS) FEM
CB (circ. CS) Analytical
CB (square CS) FEM
CB (square CS) Analytical
a)
Models with strut radius 0,25 mm
E (GPa)
Unit cells
TO FEM
TO Analytical
RD FEM
RD Analytical
DM FEM
b)
Model size 10 unit cells
v
Radius (mm)
TO FEM v12
TO Analytical v12
CB FEM v12
CB Analytical v12
c)
Model size 10 unit cells
v
Radius (mm)
RD FEM v12
RD Analytical v12
RD FEM v13
RD Analytical v13
DM FEM v12
DM FEM v13
d)
Model size 10 unit cells
E (GPa)
Radius (mm)
RD FEM
RD Analytical
TO FEM
TO Analytical
CB FEM
CB Analytical
DM FEM
e)

Figure 8

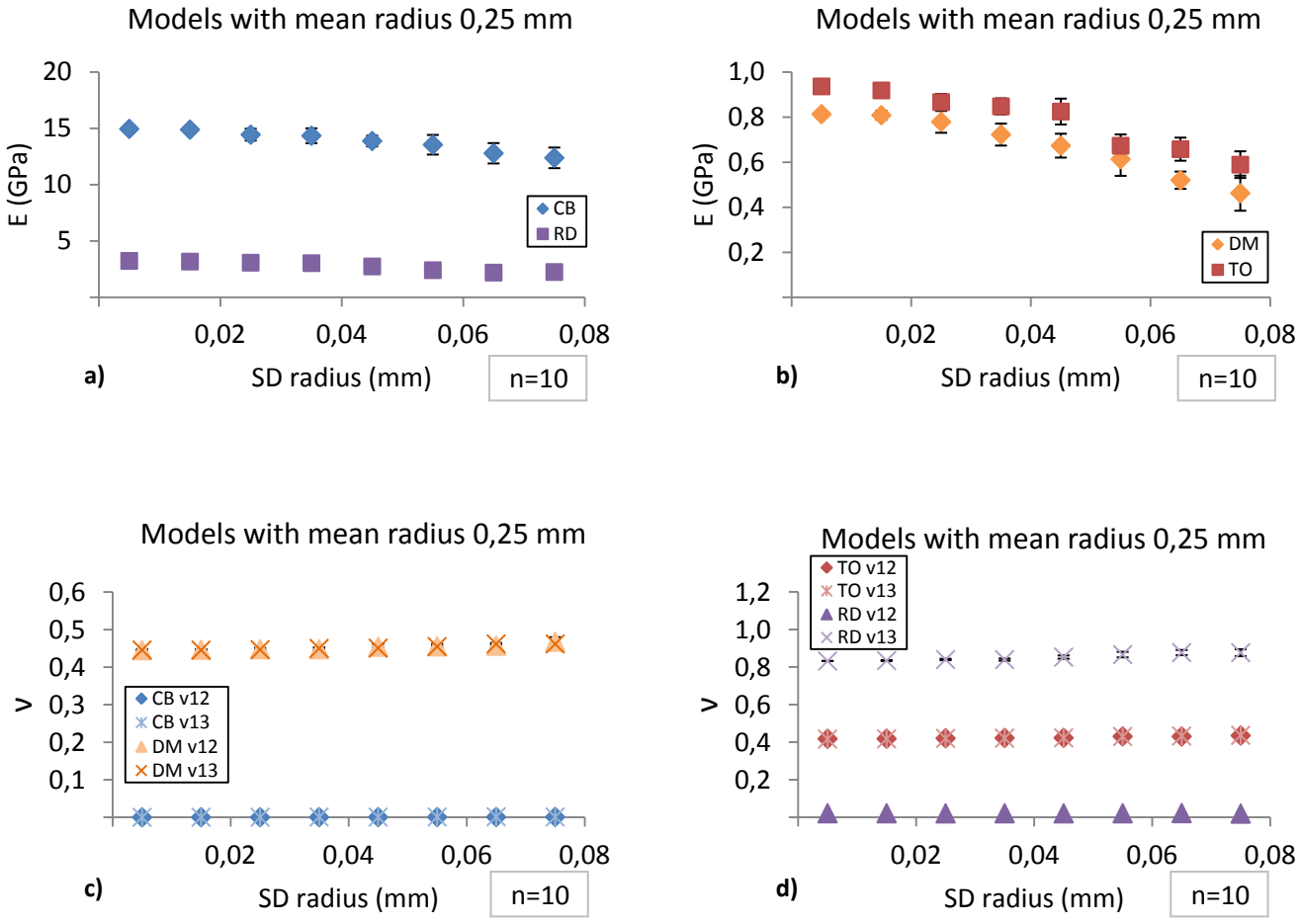
Models with mean radius 0,25 mm
E (GPa)
20
15
10
5
CB
RD
0,02
0,04
0,06
0,08
a)
SD radius (mm)
n=10
Models with mean radius 0,25 mm
E (GPa)
1,0
0,8
0,6
0,4
0,2
DM
TO
0,02
0,04
0,06
0,08
b)
SD radius (mm)
n=10
Models with mean radius 0,25 mm
v
0,6
0,5
0,4
0,3
0,2
0,1
CB v12
CB v13
DM v12
DM v13
0,02
0,04
0,06
0,08
c)
SD radius (mm)
n=10
Models with mean radius 0,25 mm
v
1,2
1,0
0,8
0,6
0,4
0,2
TO v12
TO v13
RD v12
RD v13
0,02
0,04
0,06
0,08
d)
SD radius (mm)
n=10

Figure 9

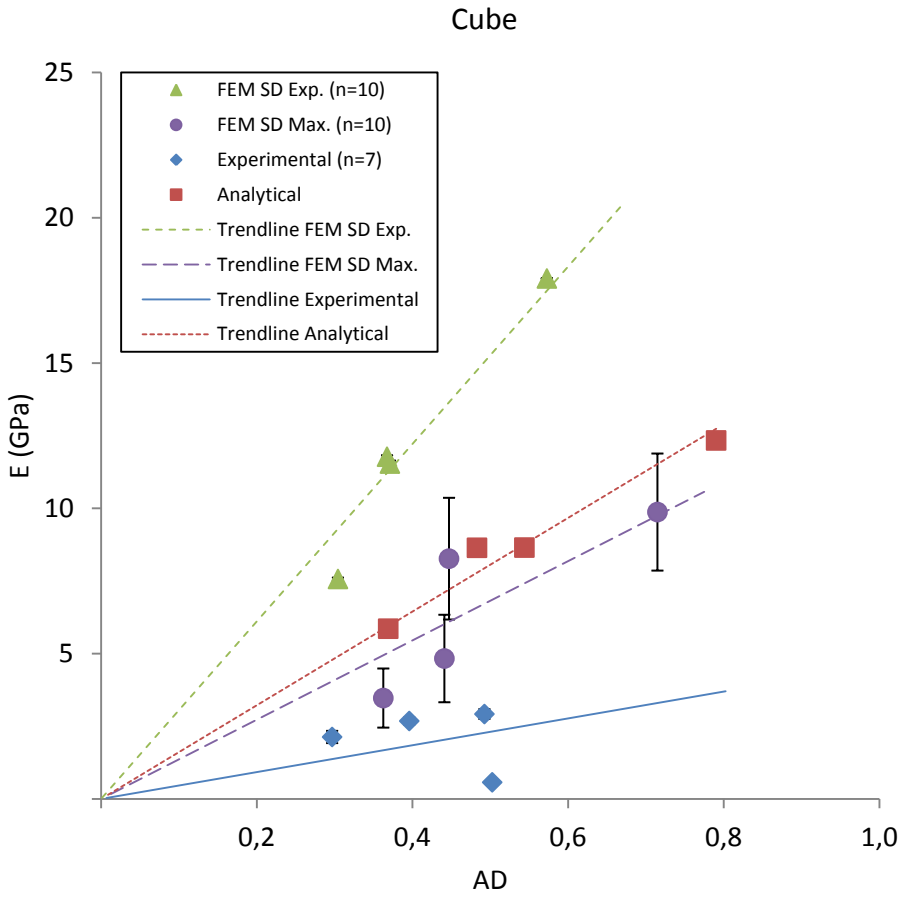
Cube
FEM SD Exp. (n=10)
FEM SD Max. (n=10)
Experimental (n=7)
Analytical
Trendline FEM SD Exp.
Trendline FEM SD Max.
Trendline Experimental
Trendline Analytical
E (GPa)
AD
25
20
15
10
5
0,2
0,4
0,6
0,8
1,0

Figure 10

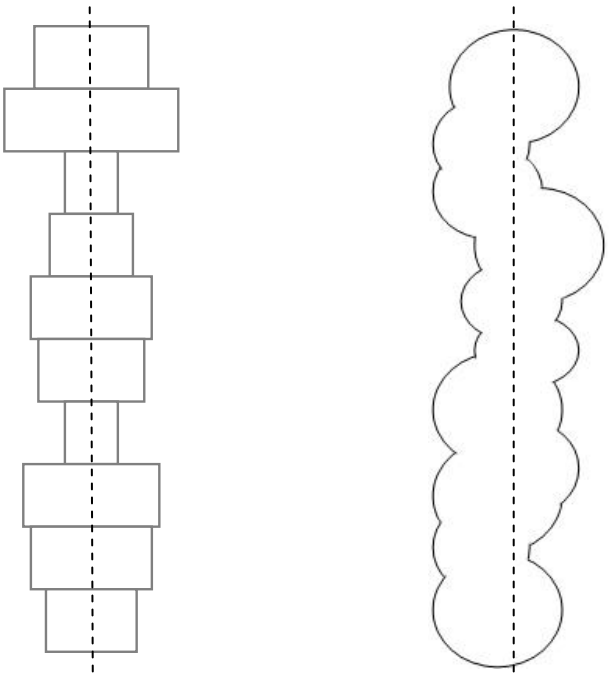

a) **b)**

Figure 11

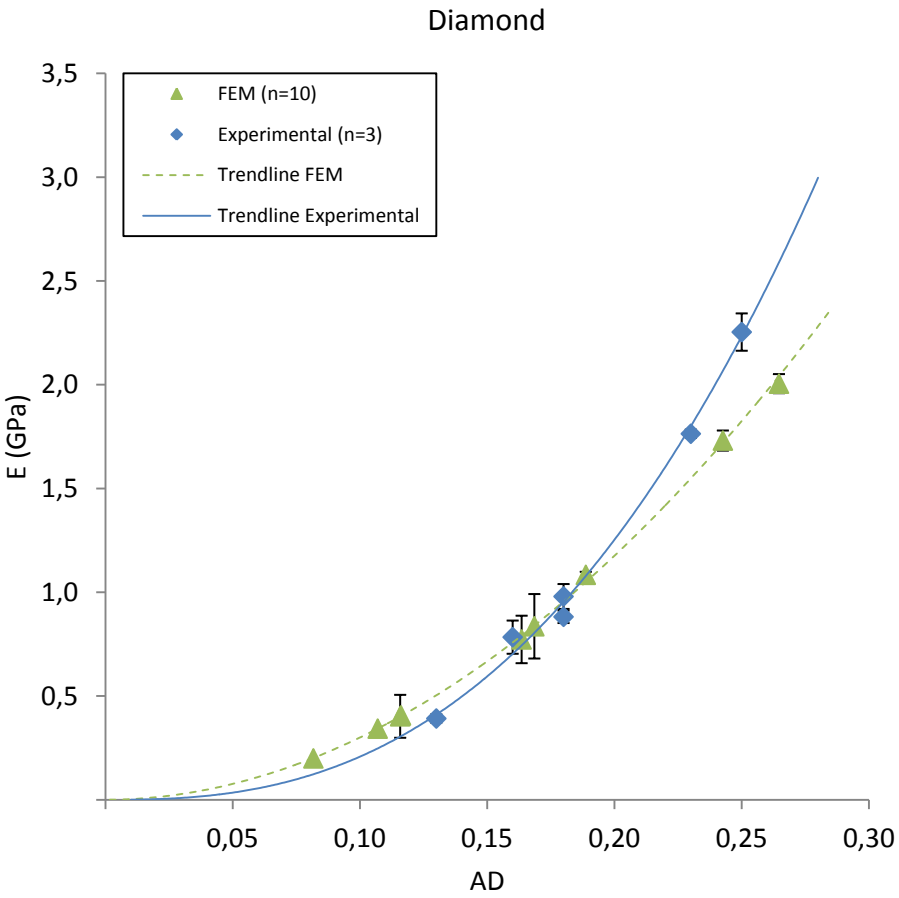
Diamond
FEM (n=10)
Experimental (n=3)
Trendline FEM
Trendline Experimental
E (GPa)
AD
3,5
3,0
2,5
2,0
1,5
1,0
0,5
0,05
0,10
0,15
0,20
0,25
0,30

Figure 12

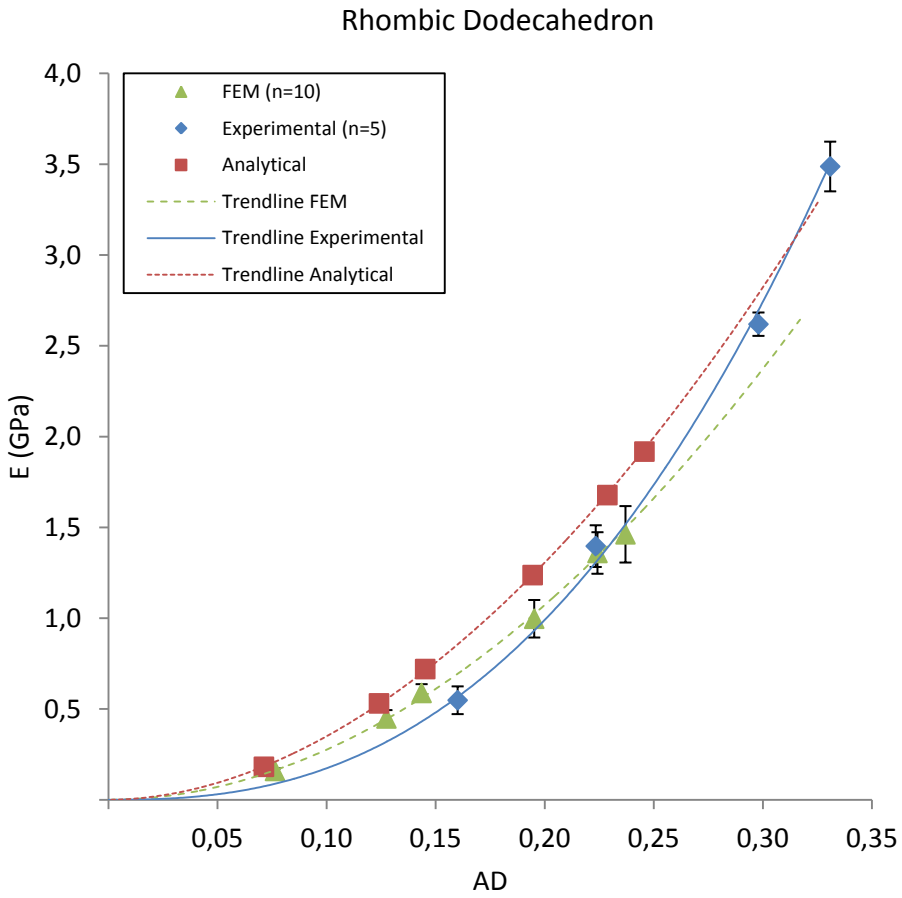
Rhombic Dodecahedron
FEM (n=10)
Experimental (n=5)
Analytical
Trendline FEM
Trendline Experimental
Trendline Analytical
E (GPa)
4,0
3,5
3,0
2,5
2,0
1,5
1,0
0,5
0,05
0,10
0,15
0,20
0,25
0,30
0,35
AD

APPENDIX 8.3.1. Additional Figures

Figure 13

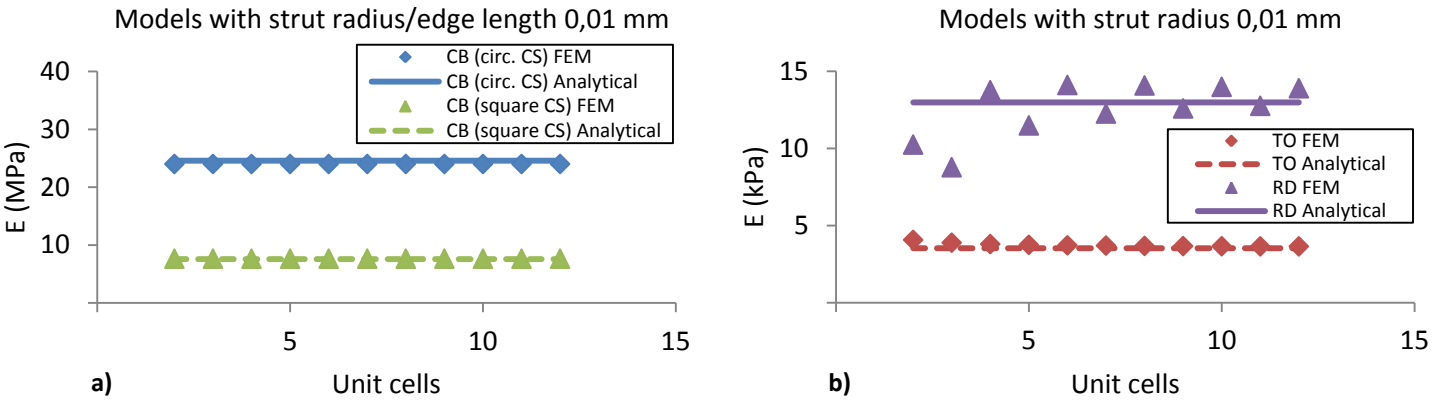

Figure 14

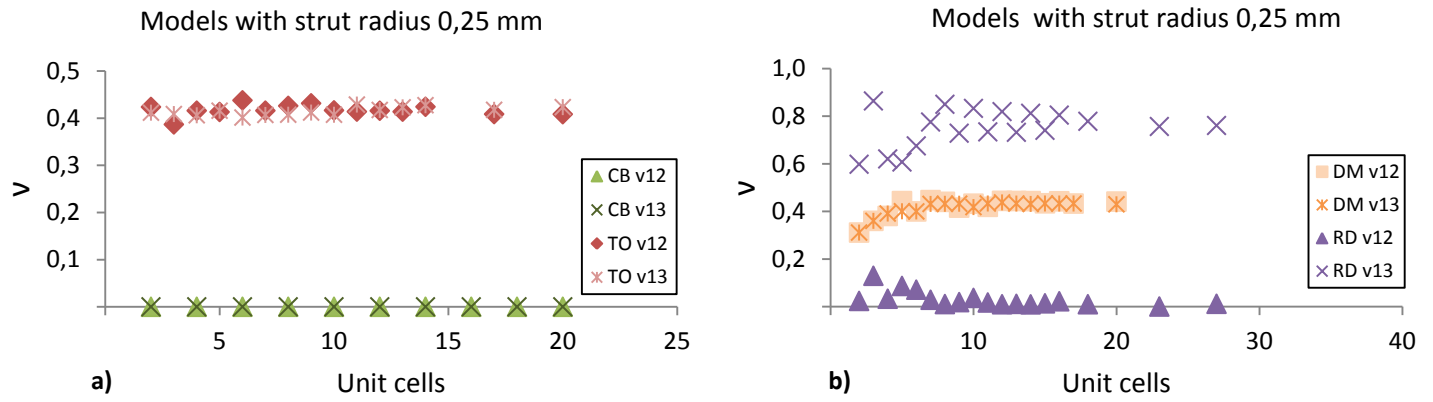

Figure 15

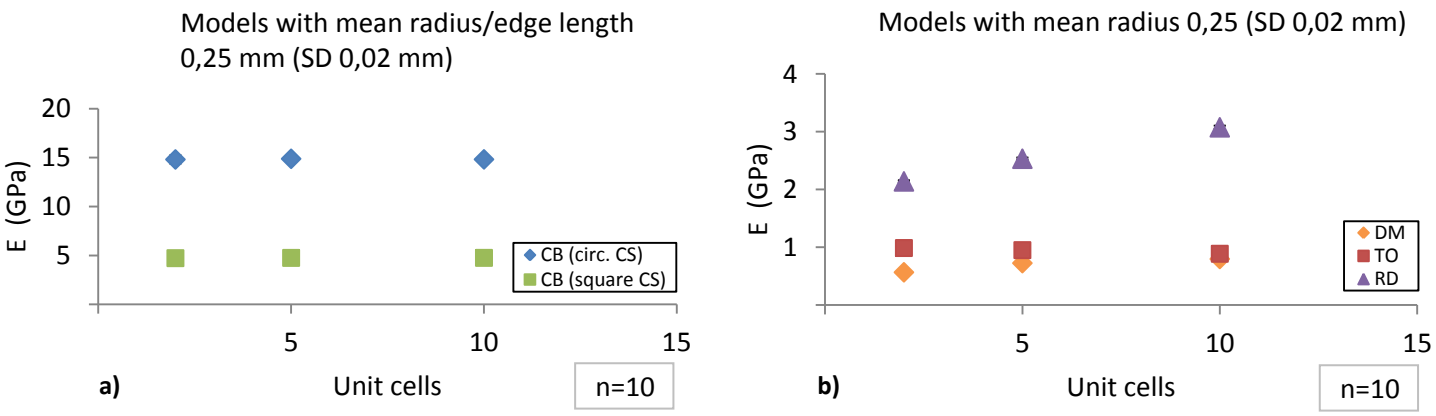

Figure 16

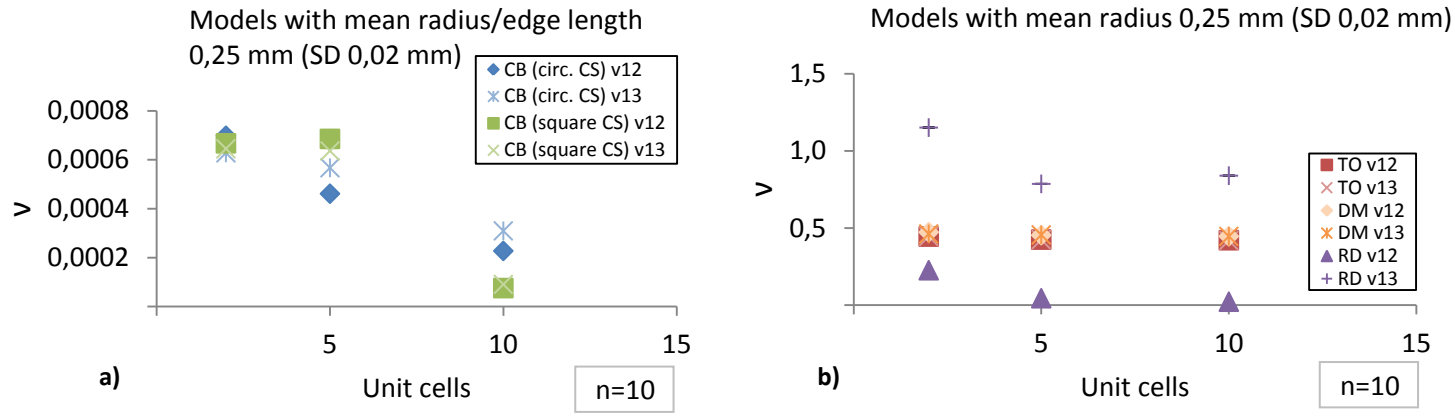

Figure 17

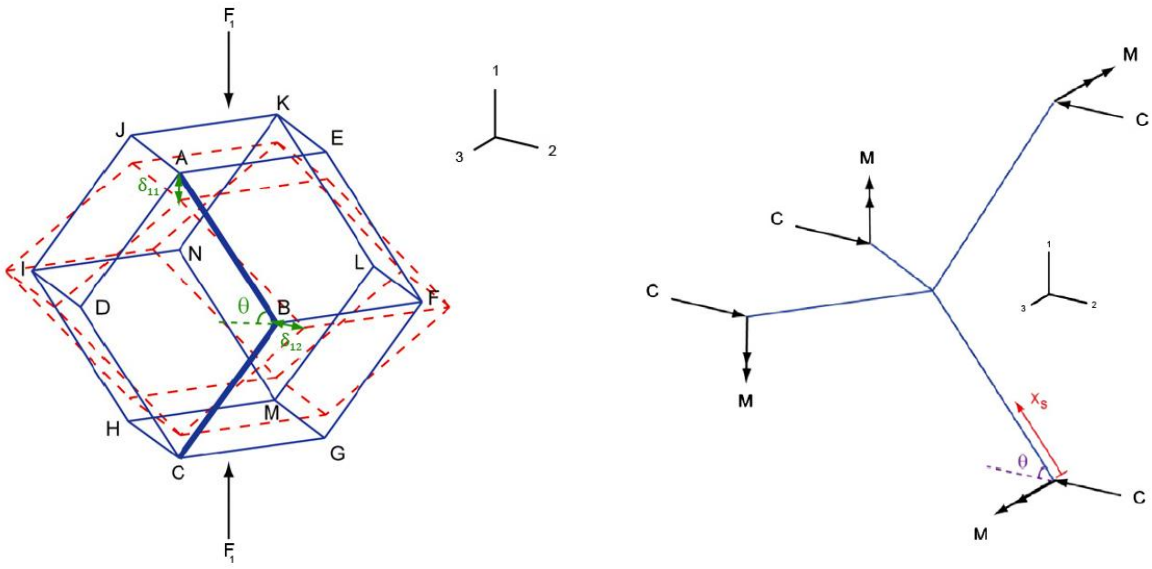
F1
K
J
E
A
δ11
N
L
D
θ
B
δ12
F
H
M
G
C
F1
1
3
2
M
C
C
M
M
C
C
M
Xs
θ

a)

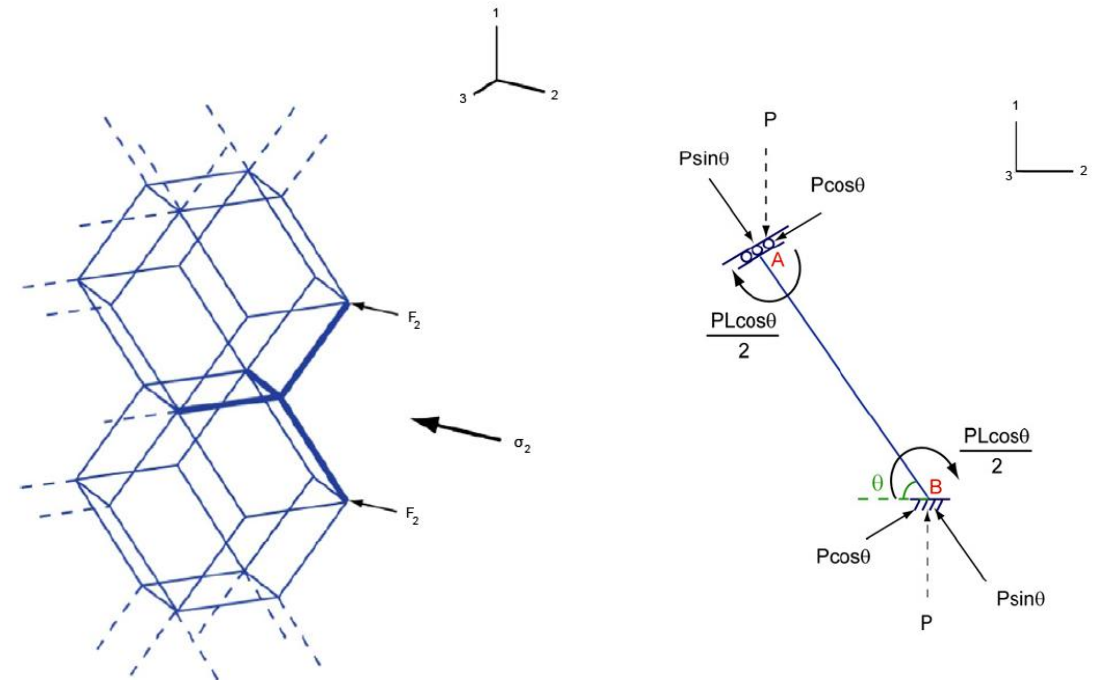
1
3
2
F2
σ2
F2
P
Psinθ
Pcosθ
A
PLcosθ
2
PLcosθ
2
θ
B
Pcosθ
Psinθ
P

b)

Table 1

Parameter	**Fixed radius**	**Gaussian distributed radius**
Young's modulus matrix material E (GPa)	110	110
Poisson's ratio matrix material ν	0.3	0.3
Beam length L (mm)	1.2	1.2
Boundary condition, direction compression	[1,0,0]	[1,0,0]
No. of divisions *elements per beam*	5	
No. of edge divisions *70 µm is the printing layer thickness in SEBM [19]*		L / 70 µm
Filter SD *mean radius ± filter · SD is allowed*		2
No. of sections variations Gaussian radius		50

Table 2

a) Experimental data cube

Set no.	Unit cells	Pore size (µm)	Experimental strut size (µm)	AD	E (GPa)	SD E (GPa)
1	7	1020 (±45)	941 (±17.1)	0.49 (±0.69)	2.92	±0.17
2	6	1424 (±42.1)	905 (±16.9)	0.40 (±0.81)	2.68	±0.12
3	5	1960 (±49.4)	882 (±13.2)	0.30 (±0.63)	2.13	±0.21
4	10	765 (±29.7)	466 (±39.7)	0.50 (±1.00)	0.57	±0.05

b) Experimental data diamond

Length (mm)	Radius (mm)	AD	Dynamic E (GPa)	Static E (GPa)	SD E (GPa)
0.9	0.21	0.29	3.0	2.9	±0.06
0.9	0.24	0.36	5.1	5.0	±0.02
0.9	0.255	0.40	6.5	6.4	±0.09
1.2	0.215	0.18	1.0	1.0	±0.02
1.2	0.255	0.23	1.8	1.8	±0.08
1.2	0.265	0.25	2.3	2.3	±0.03
1.5	0.22	0.13	0.4	0.4	±0.01
1.5	0.255	0.16	0.8	0.8	±0.02
1.5	0.27	0.18	0.9	0.9	±0.03

c) Experimental data rhombic dodecahedron

Set no.	Length (mm)	Radius (mm)	AD	E (GPa)	SD E (GPa)
1	0.749	0.067	0.16	0.549	±0.076
2	0.744	0.095	0.30	2.619	±0.064
3	0.805	0.095	0.22	1.397	±0.115
4	0.873	0.129	0.33	3.488	±0.137

Table 3

Radius (mm)	Cube			Truncated Octahedron		
	FEM AD	Hand calculation AD	Var. AD	FEM AD	Hand calculation AD	Var. AD
0.005	0.0001980	0.0001980	0.0%	0.0000607	0.0000607	0.0%
0.01	0.0007919	0.0007919	0.0%	0.0002430	0.0002430	0.0%
0.025	0.0049496	0.0049496	0.0%	0.0015186	0.0015186	0.0%
0.05	0.0197986	0.0197986	0.0%	0.0060743	0.0060743	0.0%
0.1	0.0791943	0.0791943	0.0%	0.0242970	0.0242970	0.0%
0.25	0.4949645	0.4949645	0.0%	0.1518564	0.1518564	0.0%

Table 4

Difference with UC+1	Required unit cells for stable Young's modulus			Required unit cells for stable Poisson's ratio		
Shape	< 1%	< 5%	< 10%	< 1%	< 5%	< 10%
Cube	2	2	2	2	2	2
Diamond	10	4	3	20	9	7
Truncated Octahedron	6	2	2	-	7	2
Rhombic Dodecahedron	18	16	10	-	16	14

Table 5

1a) FEM data cube (SD edge maximum, 10-20 % Vp)

Set no.	Unit cells	L (mm)	Edge (mm)	SD Edge (mm)	Min. Edge (mm)	Max. Edge (mm)	AD	E (GPa)
1	7x7x7	2.095	0.941	0.42	0.1	1.78	0.71	9.87 (±2.01)
2	6x6x6	2.480	0.905	0.40	0.1	1.71	0.44	4.83 (±1.51)
3	5x5x5	3.018	0.882	0.39	0.1	1.66	0.36	3.47 (±1.02)
4	10x10x10	1.278	0.466	0.18	0.1	0.83	0.45	8.27 (±2.09)

1b) Analytical data cube (15% Vp)

Set no.	Unit cells	L (mm)	Fixed Edge (mm)	AD	Analytical E (GPa)
1	7x7x7	2.095	0.941	0.79	12.34
2	6x6x6	2.480	0.905	0.54	8.65
3	5x5x5	3.018	0.882	0.37	5.86
4	10x10x10	1.278	0.466	0.48	8.64

1c) Comparison datasets cube

AD FEM	FEM E (GPa)	SD E (GPa)	Trendline Experimental E (GPa)	Offset FEM (%)
0.36	3.47	±1.02	1.67	107%
0.44	4.83	±1.51	2.04	137%
0.45	8.27	±2.09	2.06	300%
0.71	9.87	±2.01	3.30	199%

AD Analytical	Analytical E (GPa)	Trendline Experimental E (GPa)	Offset Analytical (%)
0.37	5.86	1.70	244%
0.48	8.64	2.23	287%
0.54	8.65	2.51	244%
0.79	12.34	3.65	238%

2a) FEM data diamond (ratio SD to mean radius 1:6)

Set no.	Unit cells	Length (mm)	Radius (mm)	SD r (mm)	Min. r (mm)	Max. r (mm)	AD	E (GPa)
1.1	31x6x7	0.9	0.21	0.035	0.14	0.28	0.19	1.08 (±0.07)
1.2	31x6x7	0.9	0.24	0.040	0.16	0.32	0.24	1.73 (±0.16)
1.3	31x6x7	0.9	0.255	0.043	0.17	0.34	0.26	2.01 (±0.09)
2.1	23x4x6	1.2	0.215	0.036	0.14	0.29	0.12	0.40 (±0.04)
2.2	23x4x6	1.2	0.255	0.043	0.17	0.34	0.16	0.77 (±0.06)
2.3	23x4x6	1.2	0.265	0.044	0.18	0.35	0.17	0.84 (±0.08)
3.1	19x4x5	1.5	0.22	0.037	0.15	0.29	0.08	0.20 (±0.03)
3.2	19x4x5	1.5	0.255	0.043	0.17	0.34	0.11	0.34 (±0.03)
3.3	19x4x5	1.5	0.27	0.045	0.18	0.36	0.12	0.41 (±0.02)

2c) Comparison datasets diamond

AD	FEM E (GPa)	Trendline Experimental E (GPa)	Offset
0.08	0.20	0.12	62%
0.11	0.34	0.25	39%
0.12	0.40	0.30	32%
0.12	0.41	0.31	33%
0.16	0.77	0.74	4%
0.17	0.84	0.80	4%
0.19	1.08	1.08	1%
0.24	1.73	2.07	-16%
0.26	2.01	2.59	-23%

3a) FEM data rhombic dodecahedron (ratio SD to mean radius 1:6)

Set no.	Unit cells	L (mm)	Radius (mm)	SD r (mm)	Min. r (mm)	Max. r (mm)	AD	FEM E (GPa)
1	12x8x10	0.749	0.067	0.012	0.044	0.090	0.08	0.16 (±0.01)
2	12x8x10	0.744	0.095	0.016	0.063	0.128	0.14	0.59 (±0.05)
3	12x6x10	0.805	0.095	0.016	0.063	0.128	0.13	0.45 (±0.05)
4	10x6x10	0.873	0.129	0.022	0.085	0.173	0.20	1.00 (±0.10)
5	12x6x10	0.805	0.129	0.022	0.085	0.173	0.22	1.36 (±0.11)
6	10x6x10	0.873	0.145	0.025	0.095	0.195	0.24	1.46 (±0.16)

3b) Analytical data rhombic dodecahedron

Set no.	Unit cells	L (mm)	Fixed radius (mm)	AD	Analytical E (GPa)
1	15x15x15	0.749	0.067	0.071	0.182
2	15x15x15	0.744	0.095	0.145	0.720
3	15x15x15	0.805	0.095	0.124	0.531
4	15x15x15	0.873	0.129	0.194	1.238
5	15x15x15	0.805	0.129	0.229	1.678
6	15x15x15	0.873	0.145	0.246	1.918

3c) Comparison datasets rhombic dodecahedron

AD FEM	FEM E (GPa)	SD E (GPa)	Trendline Experimental E (GPa)	Offset FEM (%)
0.08	0.16	±0.01	0.09	80%
0.13	0.45	±0.05	0.32	40%
0.14	0.59	±0.05	0.43	37%
0.20	1.00	±0.10	0.93	7%
0.22	1.36	±0.11	1.32	3%
0.24	1.46	±0.16	1.52	-4%

AD Analytical	Analytical E (GPa)	Trendline Experimental E (GPa)	Offset Analytical (%)
0.07	0.18	0.07	145%
0.12	0.53	0.30	78%
0.15	0.72	0.44	63%
0.19	1.24	0.92	34%
0.23	1.68	1.39	21%
0.25	1.92	1.66	15%

APPENDIX 8.3.2. Additional Tables

Table 6

a) Cube

Unitcells	E (GPa)	v_{12}	v_{13}
2	14.8 (±0.41)	0.00070 (±5.4E-7)	0.00063 (±4.0E-7)
5	14.9 (±0.28)	0.00046 (±3.6E-7)	0.00057 (±6.1E-7)
10	14.8 (±0.16)	0.00023 (±1.7E-7)	0.00031 (±1.9E-7)

b) Diamond

Unitcells	E (GPa)	v_{12}	v_{13}
2	0.569 (±0.02)	0.473 (±1.0E-5)	0.462 (±8.3E-6)
5	0.728 (±0.02)	0.453 (±2.6 E-6)	0.455 (±3.7E-6)
10	0.800 (±0.03)	0.446 (±1.8 E-6)	0.446 (±1.9E-6)

c) Truncated Octahedron

Unitcells	E (GPa)	v_{12}	v_{13}
2	0.989 (±0.03)	0.444 (±2.3E-06)	0.445 (±6.9E-06)
5	0.953 (±0.02)	0.425 (±2.1E-06)	0.424 (±2.0E-06)
10	0.890 (±0.03)	0.421 (±1.8E-06)	0.419 (±2.0E-06)

d) Rhombic Dodecahedron

Unitcells	E (GPa)	v_{12}	v_{13}
2	2.14 (±0.08)	0.226 (±2.8E-06)	1.15 (±3.5E-06)
5	2.53 (±0.10)	0.044 (±1.1E-06)	0.79 (±6.3E-06)
10	3.08 (±0.19)	0.022 (±8.2E-07)	0.84 (±6.5E-06)

Table 7

a) Cube

SD strut radius (mm)	Min. radius (mm)	Max. radius (mm)	E (GPa)	v_{12}	v_{13}
0.005	0.24	0.26	15.0 (±0.07)	4.4E-05 (±2.5E-05)	5.6E-05 (±3.5E-05)
0.015	0.22	0.28	14.9 (±0.23)	2.3E-04 (±1.5E-04)	2.1E-04 (±2.0E-04)
0.025	0.20	0.30	14.4 (±0.53)	1.8E-04 (±1.7E-04)	2.5E-04 (±1.2E-04)
0.035	0.18	0.32	14.3 (±0.66)	4.2E-04 (±4.1E-04)	9.3E-04 (±4.9E-04)
0.045	0.16	0.34	13.9 (±0.48)	5.7E-04 (±4.2E-04)	5.7E-04 (±2.0E-04)
0.055	0.14	0.36	13.5 (±0.87)	6.5E-04 (±3.2E-04)	9.9E-04 (±7.9E-04)
0.065	0.12	0.38	12.8 (±0.90)	8.2E-04 (±5.9E-04)	1.4E-03 (±1.3E-03)
0.075	0.10	0.40	12.4 (±0.91)	1.0E-03 (±6.1E-04)	7.9E-04 (±6.3E-04)

b) Diamond

SD strut radius (mm)	Min. radius (mm)	Max. radius (mm)	E (GPa)	v_{12}	v_{13}
0.005	0.24	0.26	0.813 (±7.1E-03)	0.445 (±3.7E-04)	0.446 (±4.0E-04)
0.015	0.22	0.28	0.808 (±2.0E-02)	0.446 (±1.9E-03)	0.445 (±1.1E-03)
0.025	0.20	0.30	0.779 (±4.9E-02)	0.448 (±4.2E-03)	0.447 (±3.3E-03)
0.035	0.18	0.32	0.722 (±4.9E-02)	0.448 (±3.4E-03)	0.450 (±4.3E-03)
0.045	0.16	0.34	0.673 (±5.3E-02)	0.455 (±4.2E-03)	0.451 (±6.9E-03)
0.055	0.14	0.36	0.613 (±7.4E-02)	0.456 (±5.2E-03)	0.455 (±6.1E-03)
0.065	0.12	0.38	0.520 (±3.8E-02)	0.457 (±5.1E-03)	0.462 (±3.7E-03)
0.075	0.10	0.40	0.462 (±7.8E-02)	0.468 (±1.3E-02)	0.462 (±1.2E-02)

c) Truncated Octahedron

SD strut radius (mm)	Min. radius (mm)	Max. radius (mm)	E (GPa)	v_{12}	v_{13}
0.005	0.24	0.26	0.418 (±6.4E-03)	0.418 (±1.0E-03)	0.417 (±4.2E-04)
0.015	0.22	0.28	0.419 (±2.5E-02)	0.419 (±1.6E-03)	0.418 (±1.3E-03)
0.025	0.20	0.30	0.421 (±3.6E-02)	0.421 (±2.7E-03)	0.420 (±2.3E-03)
0.035	0.18	0.32	0.423 (±3.6E-02)	0.423 (±2.7E-03)	0.422 (±3.1E-03)
0.045	0.16	0.34	0.423 (±5.8E-02)	0.423 (±3.9E-03)	0.423 (±3.5E-03)
0.055	0.14	0.36	0.431 (±5.0E-02)	0.431 (±4.3E-03)	0.431 (±5.2E-03)
0.065	0.12	0.38	0.431 (±5.1E-02)	0.431 (±3.9E-03)	0.433 (±6.5E-03)
0.075	0.10	0.40	0.436 (±5.9E-02)	0.436 (±5.2E-03)	0.437 (±7.1E-03)

d) Rhombic Dodecahedron

SD strut radius (mm)	Min. radius (mm)	Max. radius (mm)	E (GPa)	v_{12}	v_{13}
0.005	0.24	0.26	3.23 (±0.03)	0.022 (±2.2E-04)	0.833 (±7.3E-04)
0.015	0.22	0.28	3.17 (±0.06)	0.022 (±6.7E-04)	0.835 (±2.2E-03)
0.025	0.20	0.30	3.07 (±0.13)	0.021 (±8.7E-04)	0.841 (±3.9E-03)
0.035	0.18	0.32	3.03 (±0.13)	0.022 (±1.0E-03)	0.840 (±6.1E-03)
0.045	0.16	0.34	2.74 (±0.23)	0.021 (±2.5E-03)	0.853 (±8.8E-03)
0.055	0.14	0.36	2.40 (±0.36)	0.022 (±3.5E-03)	0.867 (±1.5E-02)
0.065	0.12	0.38	2.19 (±0.31)	0.023 (±4.2E-03)	0.877 (±1.4E-02)
0.075	0.10	0.40	2.24 (±0.40)	0.020 (±3.0E-03)	0.877 (±1.9E-02)

Table 8

a)

Edge (mm)	0.01		**FEM**	**Gent & Thomas**	
Unit cells		AD	E (MPa)	E (MPa)	Variation
2		0.000469	7.64	7.58	1%
3		0.000370	7.64	7.58	1%
4		0.000326	7.64	7.58	1%
5		0.000300	7.64	7.58	1%
6		0.000284	7.64	7.58	1%
7		0.000272	7.64	7.58	1%
8		0.000264	7.64	7.58	1%
9		0.000257	7.64	7.58	1%
10		0.000252	7.64	7.58	1%

b)

Edge (mm)	0.25		**FEM**	**Gent & Thomas**	
Unit cells		AD	E (GPa)	E (GPa)	Variation
2		0.293	4.77	3.95	21%
3		0.231	4.77	3.95	21%
4		0.203	4.77	3.95	21%
5		0.188	4.77	3.95	21%
6		0.177	4.77	3.95	21%
7		0.170	4.77	3.95	21%
8		0.165	4.77	3.95	21%
9		0.161	4.77	3.95	21%
10		0.158	4.77	3.95	21%

c)

Unit cells	10	**FEM**	**Gent & Thomas**	Variation
Edge (mm)		E (MPa)	E (MPa)	E
0.005		1.91	1.90	0%
0.01		7.64	7.58	1%
0.025		47.74	46.77	2%
0.05		190.97	183.33	4%
0.1		763.89	705.13	8%
0.25		4774.31	3951.15	21%

Table 9

a)

Radius (mm)	0.01			**FEM**		**Gent & Thomas**		
Unit cells		AD FEM	AD INF.	E (MPa)	ν	*Beta*	E (MPa)	Variation
2		0.001473	0.000654	24.00	0.0	*0.015062*	24.58	-2.4%
3		0.001164	0.000654	24.00	0.0	*0.015062*	24.58	-2.4%
4		0.001023	0.000654	24.00	0.0	*0.015062*	24.58	-2.4%
5		0.000942	0.000654	24.00	0.0	*0.015062*	24.58	-2.4%
6		0.000891	0.000654	24.00	0.0	*0.015062*	24.58	-2.4%
7		0.000855	0.000654	24.00	0.0	*0.015062*	24.58	-2.4%
8		0.000828	0.000654	24.00	0.0	*0.015062*	24.58	-2.4%
9		0.000808	0.000654	24.00	0.0	*0.015062*	24.58	-2.4%
10		0.000792	0.000654	24.00	0.0	*0.015062*	24.58	-2.4%

b)

Radius (mm)	0.25			**FEM**		**Gent & Thomas**		
Unit cells		AD FEM	AD INF.	E (GPa)	ν	*Beta*	E (GPa)	Variation
2		0.9204	0.4091	15.00	0.0	*0.782845*	37.81	-60.3%
3		0.7272	0.4091	15.00	0.0	*0.782845*	37.81	-60.3%
4		0.6392	0.4091	15.00	0.0	*0.782845*	37.81	-60.3%
5		0.5890	0.4091	15.00	0.0	*0.782845*	37.81	-60.3%
6		0.5568	0.4091	15.00	0.0	*0.782845*	37.81	-60.3%
7		0.5343	0.4091	15.00	0.0	*0.782845*	37.81	-60.3%
8		0.5177	0.4091	15.00	0.0	*0.782845*	37.81	-60.3%
9		0.5050	0.4091	15.00	0.0	*0.782845*	37.81	-60.3%
10		0.4950	0.4091	15.00	0.0	*0.782845*	37.81	-60.3%

c)

Unit cells	10x10x10			**FEM**		**Gent & Thomas**		Variation
Radius (mm)		AD FEM	AD INF.	E (MPa)	ν	*Beta*	E (MPa)	E
0.005		0.0001980	0.0001636	6	0.0	*0.007467*	6.09	-1.5%
0.01		0.0007919	0.0006545	24	0.0	*0.015062*	24.58	-2.4%
0.025		0.0049496	0.0040906	150	0.0	*0.038850*	159.82	-6.1%
0.05		0.0197986	0.0163625	600	0.0	*0.082006*	683.68	-12.2%
0.1		0.0791943	0.0654498	2400	0.0	*0.184896*	3173.71	-24.4%
0.25		0.4949645	0.4090615	14999	0.0	*0.782764*	37805.95	-60.3%

Table 10

a)

Radius (mm)	0.01	**FEM**		
Unit cells		E (kPa)	v12	v13
2		2.64	0.52	0.52
3		2.76	0.51	0.50
4		2.85	0.51	0.51
5		2.91	0.51	0.50
6		2.95	0.51	0.51
7		2.99	0.51	0.51
8		3.02	0.51	0.51
9		3.04	0.51	0.51
10		3.06	0.51	0.51
11		3.08	0.51	0.51
12		3.09	0.51	0.51
13		3.11	0.51	0.50
14		3.12	0.51	0.51
15		3.13	0.51	0.51
16		2.08	0.52	0.52
17		2.44	0.52	0.50
20		3.15	0.51	0.51

b)

Radius (mm)	0.25	**FEM**		
Unit cells		E (GPa)	v12	v13
2		0.59	0.31	0.31
3		0.68	0.36	0.36
4		0.73	0.38	0.39
5		0.76	0.44	0.40
6		0.78	0.40	0.40
7		0.79	0.45	0.43
8		0.80	0.44	0.43
9		0.81	0.42	0.43
10		0.82	0.43	0.42
11		0.83	0.42	0.43
12		0.83	0.44	0.44
13		0.83	0.44	0.43
14		0.84	0.44	0.43
15		0.84	0.43	0.43
16		0.84	0.44	0.43
17		0.85	0.43	0.43
20		0.85	0.44	0.43

c)

Unit cells	10x10x10	**FEM**		
Radius (mm)		E (MPa)	v12	v13
0.005		0.00	0.50	0.48
0.01		0.00	0.50	0.48
0.025		0.12	0.50	0.48
0.05		1.85	0.49	0.48
0.1		28.22	0.48	0.47
0.25		819.93	0.43	0.42

Table 11

a)

Radius (mm)	0.01			**FEM**			**Roberts & Garboczi**		Variation		
Unit cells		AD FEM	AD INF.	E (kPa)	v12	v13	E (kPa)	v12/v13	E	v12	v13
2		0.000289	0.000231	4.07	0.492	0.507	3.54	0.50	15%	-2%	2%
3		0.000270	0.000231	3.89	0.464	0.499	3.54	0.50	10%	-7%	0%
4		0.000260	0.000231	3.80	0.504	0.495	3.54	0.50	7%	1%	-1%
5		0.000255	0.000231	3.75	0.500	0.498	3.54	0.50	6%	0%	0%
6		0.000251	0.000231	3.72	0.516	0.488	3.54	0.50	5%	3%	-2%
7		0.000248	0.000231	3.70	0.491	0.495	3.54	0.50	4%	-2%	-1%
8		0.000246	0.000231	3.68	0.511	0.495	3.54	0.50	4%	2%	-1%
9		0.000244	0.000231	3.67	0.513	0.497	3.54	0.50	3%	3%	-1%
10		0.000243	0.000231	3.66	0.504	0.495	3.54	0.50	3%	1%	-1%
11		0.000242	0.000231	3.65	0.498	0.509	3.54	0.50	3%	0%	2%
12		0.000241	0.000231	3.65	0.503	0.503	3.54	0.50	3%	1%	1%
13		0.000240	0.000231	3.64	0.498	0.506	3.54	0.50	3%	0%	1%
14		0.000240	0.000231	3.63	0.505	0.509	3.54	0.50	3%	1%	2%
17		0.000238	0.000231	3.62	0.491	0.503	3.54	0.50	2%	-2%	1%
20		0.000237	0.000231	3.62	0.492	0.506	3.54	0.50	2%	-2%	1%

b)

Radius (mm)	0.25			**FEM**			**Roberts & Garboczi**		Variation		
Unit cells		AD FEM	AD INF.	E (GPa)	v12	v13	E (GPa)	v12/v13	E	v12	v13
2		0.1808	0.1446	1.02	0.42	0.41	1.22	0.38	-17%	10%	7%
3		0.1687	0.1446	0.98	0.39	0.41	1.22	0.38	-20%	0%	6%
4		0.1627	0.1446	0.97	0.42	0.41	1.22	0.38	-21%	8%	6%
5		0.1591	0.1446	0.96	0.41	0.42	1.22	0.38	-22%	7%	8%
6		0.1567	0.1446	0.95	0.44	0.40	1.22	0.38	-22%	14%	4%
7		0.1550	0.1446	0.95	0.42	0.41	1.22	0.38	-23%	8%	6%
8		0.1537	0.1446	0.94	0.43	0.41	1.22	0.38	-23%	11%	6%
9		0.1527	0.1446	0.94	0.43	0.41	1.22	0.38	-23%	12%	7%
10		0.1519	0.1446	0.94	0.42	0.41	1.22	0.38	-23%	8%	6%
11		0.1512	0.1446	0.94	0.41	0.43	1.22	0.38	-23%	8%	11%
12		0.1507	0.1446	0.94	0.42	0.42	1.22	0.38	-23%	8%	8%
13		0.1502	0.1446	0.93	0.41	0.42	1.22	0.38	-24%	8%	10%
14		0.1498	0.1446	0.93	0.42	0.43	1.22	0.38	-24%	10%	11%
17		0.1489	0.1446	0.93	0.41	0.42	1.22	0.38	-24%	6%	9%
20		0.1482	0.1446	0.93	0.41	0.42	1.22	0.38	-24%	6%	10%

c)

Unit cells	10			**FEM**			**Roberts & Garboczi**		Variation		
Radius (mm)		AD FEM	AD INF.	E (MPa)	v12	v13	E (MPa)	v12/v13	E	v12	v13
0.005		0.000061	0.000058	0.0002	0.50	0.49	0.0002	0.50	4%	1%	-1%
0.01		0.000243	0.000231	0.0037	0.50	0.49	0.0035	0.50	3%	1%	-1%
0.025		0.001519	0.001446	0.1424	0.50	0.49	0.1379	0.50	3%	1%	-1%
0.05		0.006074	0.005785	2.2420	0.50	0.49	2.1973	0.49	2%	1%	-1%
0.1		0.024297	0.023140	33.7658	0.48	0.47	34.6196	0.48	-3%	1%	-1%
0.25		0.151856	0.144625	938.7419	0.42	0.41	1221.50	0.38	-23%	8%	6%

Table 12

a)

Radius (mm)	0.01		**FEM** (1st direction)			**Babaee** (2nd /3rd dir.)			Variation		
Unit cells		AD	E (kPa)	v12	v13	E (kPa)	v12	v13	E	v12	v13
2		0.001204	10.25	0.13	0.86	12.98	0	1	-21%	-	-14%
3		0.000724	8.78	0.10	1.05	12.98	0	1	-32%	-	5%
4		0.000903	13.77	0.05	0.89	12.98	0	1	6%	-	-11%
5		0.000692	11.49	0.09	0.82	12.98	0	1	-11%	-	-18%
6		0.000795	14.11	0.07	0.95	12.98	0	1	9%	-	-5%
7		0.000665	12.26	0.00	0.98	12.98	0	1	-6%	-	-2%
8		0.000740	14.08	0.00	1.09	12.98	0	1	8%	-	9%
9		0.000647	12.59	0.01	0.96	12.98	0	1	-3%	-	-4%
10		0.000706	13.99	0.03	1.07	12.98	0	1	8%	-	7%
11		0.000635	12.76	0.02	0.97	12.98	0	1	-2%	-	-3%
12		0.000683	13.90	0.01	1.06	12.98	0	1	7%	-	6%

b)

Radius (mm)	0.25		**FEM** (1st direction)			**Babaee** (2nd /3rd dir.)			Variation		
Unit cells		AD	E (GPa)	v12	v13	E (GPa)	v12	v13	E	v12	v13
2		0.753	2.21	0.21	1.15	4.02	0	1	-45%	-	15%
3		0.453	1.94	0.12	0.86	4.02	0	1	-52%	-	-14%
4		0.565	3.08	0.04	0.95	4.02	0	1	-23%	-	-5%
5		0.432	2.60	0.04	0.78	4.02	0	1	-35%	-	-22%
6		0.497	3.23	0.03	0.88	4.02	0	1	-20%	-	-12%
7		0.416	2.82	0.02	0.77	4.02	0	1	-30%	-	-23%
8		0.462	3.26	0.02	0.85	4.02	0	1	-19%	-	-15%
9		0.405	2.92	0.02	0.76	4.02	0	1	-27%	-	-24%
10		0.441	3.26	0.02	0.83	4.02	0	1	-19%	-	-17%
11		0.397	2.98	0.02	0.76	4.02	0	1	-26%	-	-24%
12		0.427	3.25	0.02	0.82	4.02	0	1	-19%	-	-18%

c)

Radius (mm)	0.01		**FEM** (3rd direction)			**Babaee** (1st dir.)			Variation		
Unit cells		AD	E (MPa)	v31	v32	E (MPa)	v12	v13	E	v31	v32
2		0.001204	0.0046	0.41	0.41	0.0065	0.5	0.5	-30%	-18%	-17%
3		0.000724	0.0073	0.56	0.55	0.0065	0.5	0.5	13%	12%	10%
4		0.000903	0.0062	0.44	0.43	0.0065	0.5	0.5	-4%	-11%	-15%
5		0.000692	0.0076	0.54	0.51	0.0065	0.5	0.5	17%	8%	2%
6		0.000795	0.0065	0.45	0.43	0.0065	0.5	0.5	17%	-10%	-14%
7		0.000665	0.0075	0.53	0.52	0.0065	0.5	0.5	15%	5%	3%
8		0.000740	0.0066	0.47	0.45	0.0065	0.5	0.5	2%	-6%	-10%
9		0.000647	0.0073	0.52	0.50	0.0065	0.5	0.5	13%	5%	0%
10		0.000706	0.0066	0.47	0.45	0.0065	0.5	0.5	2%	-5%	-9%
11		0.000635	0.0072	0.52	0.50	0.0065	0.5	0.5	11%	4%	0%
12		0.000683	0.0067	0.47	0.46	0.0065	0.5	0.5	2%	-6%	-8%

d)

Radius (mm)	0.25		**FEM** (3rd direction)			**Babaee** (1st dir.)			Variation		
Unit cells		AD	E (GPa)	v31	v32	E (GPa)	v31	v32	E	v31	v32
2		0.753	1.177	0.38	0.38	2.54	0.5	0.5	-54%	-25%	-25%
3		0.453	1.860	0.48	0.48	2.54	0.5	0.5	-27%	-4%	-4%
4		0.565	1.618	0.39	0.36	2.54	0.5	0.5	-36%	-21%	-28%
5		0.432	1.982	0.47	0.44	2.54	0.5	0.5	-22%	-7%	-12%
6		0.497	1.717	0.39	0.37	2.54	0.5	0.5	-22%	-22%	-26%
7		0.416	1.972	0.45	0.44	2.54	0.5	0.5	-22%	-9%	-11%
8		0.462	1.751	0.40	0.38	2.54	0.5	0.5	-31%	-19%	-23%
9		0.405	1.949	0.45	0.43	2.54	0.5	0.5	-23%	-10%	-14%
10		0.441	1.766	0.40	0.39	2.54	0.5	0.5	-30%	-20%	-22%
11		0.397	1.928	0.45	0.43	2.54	0.5	0.5	-24%	-11%	-14%
12		0.427	1.774	0.40	0.40	2.54	0.5	0.5	-30%	-19%	-20%

e)

Unit cells	10		**FEM** (1st direction)			**Babaee** (2nd/3rd dir.)			Variation		
Radius (mm)		AD	E (MPa)	v12	v13	E (MPa)	v32	v31	E	v12	v13
0.005		0.00018	0.00088	0.009	1.073	0.00081	0.0	1.0	8%	-	7%
0.01		0.00071	0.01399	0.010	1.072	0.01298	0.0	1.0	8%	-	7%
0.025		0.00441	0.54203	0.011	1.067	0.50586	0.0	1.0	7%	-	7%
0.05		0.01764	8.47949	0.014	1.054	8.03111	0.0	1.0	6%	-	5%
0.1		0.07057	125.469	0.017	1.014	124.643	0.0	1.0	1%	-	1%
0.25		0.44105	3260.58	0.024	0.831	4023.85	0.0	1.0	-19%	-	-17%

f)

Unit cells	10		**FEM** (3rd direction)			**Babaee** (1st dir.)			Variation		
Radius (mm)		AD	E (MPa)	v12	v13	E (MPa)	v32	v31	E	v12	v13
0.005		0.00018	0.00042	0.47	0.45	0.00041	0.5	0.5	3%	-5%	-9%
0.01		0.00071	0.00664	0.47	0.45	0.00650	0.5	0.5	2%	-5%	-9%
0.025		0.00441	0.25808	0.47	0.45	0.25393	0.5	0.5	2%	-5%	-10%
0.05		0.01764	4.06829	0.47	0.45	4.06284	0.5	0.5	0%	-6%	-10%
0.1		0.07057	61.6188	0.46	0.44	65.0054	0.5	0.5	-5%	-8%	-12%
0.25		0.44105	1766.37	0.41	0.39	2539.27	0.5	0.5	-30%	-18%	-22%